

**STAG2 promotes the myelination transcriptional program  
in oligodendrocytes**

Ningyan Cheng<sup>1</sup>, Guanchen Li<sup>2,3,4</sup>, Mohammed Kanchwala<sup>5</sup>, Bret M. Evers<sup>6</sup>, Chao Xing<sup>5,7</sup>,  
Hongtao Yu<sup>1,2,3,4,\*</sup>

<sup>1</sup>Department of Pharmacology, University of Texas Southwestern Medical Center, Dallas, TX  
75390, USA.

<sup>2</sup>Westlake Laboratory of Life Sciences and Biomedicine, Hangzhou, China.

<sup>3</sup>School of Life Sciences, Westlake University, Hangzhou, China.

<sup>4</sup>Institute of Biology, Westlake Institute for Advanced Study, Hangzhou, China.

<sup>5</sup>Eugene McDermott Center for Human Growth and Development, University of Texas  
Southwestern Medical Center, Dallas, TX 75390, USA.

<sup>6</sup>Division of Neuropathology, University of Texas Southwestern Medical Center, Dallas, TX,  
75390, USA.

<sup>7</sup>Department of Bioinformatics, Department of Population and Data Sciences, University of  
Texas Southwestern Medical Center, Dallas, TX 75390, USA.

\*Correspondence: yuhongtao@westlake.edu.cn

## 21   **Abstract**

22   Cohesin folds chromosomes via DNA loop extrusion. Cohesin-mediated chromosome loops  
23   regulate transcription by shaping long-range enhancer-promoter interactions, among other  
24   mechanisms. Mutations of cohesin subunits and regulators cause human developmental diseases  
25   termed cohesinopathy. Vertebrate cohesin consists of SMC1, SMC3, RAD21, and either STAG1  
26   or STAG2. To probe the physiological functions of cohesin, we created conditional knockout  
27   (cKO) mice with *Stag2* deleted in the nervous system. *Stag2* cKO mice exhibit growth  
28   retardation, neurological defects, and premature death, in part due to insufficient myelination of  
29   nerve fibers. *Stag2* cKO oligodendrocytes exhibit delayed maturation and downregulation of  
30   myelination-related genes. *Stag2* loss reduces promoter-anchored loops at downregulated genes  
31   in oligodendrocytes. Thus, STAG2-cohesin generates promoter-anchored loops at myelination-  
32   promoting genes to facilitate their transcription. Our study implicates defective myelination as a  
33   contributing factor to cohesinopathy and establishes oligodendrocytes as a relevant cell type to  
34   explore the mechanisms by which cohesin regulates transcription.

35

## Introduction

Chromosomes in a single human diploid cell, if linearly stitched together, span a length of more than two meters. They need to be properly folded to be housed in the cell nucleus with a diameter of 10  $\mu\text{m}$ . Chromosome folding occurs in a dynamic, structured way that regulates gene expression, and DNA replication and repair. Initially discovered as the molecular glue that tethers sister chromatids for segregation during mitosis (Haarhuis et al., 2014; Uhlmann, 2016; Yatskevich et al., 2019; Zheng and Yu, 2015), the cohesin complex has later been shown to be critical for structured chromosome folding and gene expression (Haarhuis et al., 2017; Rao et al., 2017; Schwarzer et al., 2017; Wutz et al., 2017).

Cohesin is loaded on chromosomes by the cohesin loader NIPBL. The cohesin–NIPBL complex can extrude DNA loops bi-directionally in an ATP-dependent manner (Davidson et al., 2019; Kim et al., 2019; Vian et al., 2018). The chromatin insulator CTCF has been proposed to block loop extrusion by cohesin, establishing topologically associated domains (TADs) and marking TAD boundaries. Chromatin interactions within each TAD are favored whereas inter-TAD interactions are disfavored. Thus, chromosome loops and TADs shape long-range cis-element interactions, such as promoter-enhancer interactions, thereby regulating transcription.

The vertebrate cohesin complex contains four core subunits: the SMC1–SMC3 heterodimeric ATPase, the kleisin subunit RAD21 that links the ATPase heads, and the HEAT-repeat protein STAG1 or STAG2. STAG1 and STAG2 bind to RAD21 in a mutually exclusive manner and create docking sites for several regulatory proteins, including CTCF (Hara et al., 2014; Li et al., 2020). STAG1 and STAG2 also interact with DNA and the SMC1–SMC3 hinge domains (Shi et al., 2020). STAG1 and STAG2 play redundant roles in sister-chromatid

cohesion in cultured human cells, as both need to be simultaneously depleted to produce overt cohesion defects (Hara et al., 2014).

Mutations of NIPBL and cohesin subunits, including STAG2, result in human developmental diseases termed cohesinopathies, which affect multiple organs and systems (Remeseiro et al., 2013b; Soardi et al., 2017). In patients with cohesinopathies, mental retardation and neurological abnormalities caused by brain development defects are common (Piche et al., 2019). Dysregulation of gene transcription as a result of reduced cohesin functions has been suggested to underlie these developmental defects (De Koninck and Losada, 2016; Remeseiro et al., 2013a). In addition, several cohesin genes, including *STAG2*, are frequently mutated in a variety of human cancers (Martincorena and Campbell, 2015).

In this study, we deleted *Stag2* specifically in the nervous system in the mouse. The *Stag2* conditional knockout (cKO) mice exhibited deficient myelination. Loss of STAG2 delayed the maturation of oligodendrocytes and reduced chromosome loops in oligodendrocytes and impaired the transcription of myelination-related genes. Our findings establish the requirement for cohesin in proper gene expression in specific cell types and implicate defective myelination as a potential contributing factor to cohesinopathy.

## Results

### ***Stag2* ablation in the nervous system causes growth retardation and neurological defects**

*Stag1* is required for mammalian embryonic development (Remeseiro et al., 2012), indicating that *Stag2* cannot compensate for the loss of *Stag1*. To examine the physiological functions of *Stag2* in the mouse, we created a *Stag2* “floxed” mouse line (*Stag2<sup>ff</sup>*) by homologous recombination with a template that contained two LoxP sites flanking exon 8 (Figure 1A,B) and targeted a critical exon (exon 8) of *Stag2*, which is located on the X chromosome, using CRISPR-Cas9 (Figure 1—Figure Supplement 1A). The *Stag2<sup>null</sup>* embryos showed severe developmental defects and underwent necrosis by E11.5 days (Figure 1—Figure Supplement 1B). Thus, *Stag2* is required for mouse embryonic development, consistent with a previous report (De Koninck et al., 2020). *Stag1* and *Stag2* have non-redundant developmental functions.

To study the functions of STAG2 in adult mice, we crossed the *Stag2<sup>ff</sup>* mice with mice bearing the *Rosa26<sup>CreErt2</sup>* genomic insertion and generated *Stag2<sup>ff/y</sup>;Rosa26<sup>CreErt2</sup>* progenies. The *Stag2<sup>ff/y</sup>;Rosa26<sup>CreErt2</sup>* adult mice were injected with tamoxifen to induce *Stag2* deletion in the whole body (Figure 1—Figure Supplement 2A). Genotyping analysis of blood extracts showed that tamoxifen induced efficient disruption of the *Stag2* gene locus in *Stag2<sup>ff/y</sup>;Rosa26<sup>CreErt2</sup>* mice (Figure 1—Figure Supplement 2B,C). These *Stag2*-deficient adult mice did not show early onset of spontaneous tumor formation, indicating that *Stag2* mutation alone in somatic cells of mice is insufficient to induce tumorigenesis. The *Stag2*-deficient mice also did not have other obvious adverse phenotypes (Figure 1—Figure Supplement 2D), except that they had slightly lower body weight (Figure 1—Figure Supplement 2E,F), probably due to tissue homeostasis alterations reported by others (De Koninck et al., 2020).

STAG2 mutations are found in human cohesinopathy patients with mental retardation and neuropsychiatric behaviors (Soardi et al., 2017). To study the function of STAG2 in the nervous system, we generated *Stag2* conditional knockout mice (*Stag2* cKO) by crossing *Stag2<sup>ff</sup>* mice with Nestin-Cre mice (Giusti et al., 2014) (Figure 1C,D). The progenies were born in the Mendelian ratio, but *Stag2<sup>ff/y</sup>;Nes<sup>Cre</sup>* pups presented growth retardation and premature death (Figure 1E,G). More than 50% *Stag2<sup>ff/y</sup>;Nes<sup>Cre</sup>* mice died aged about 3 weeks while the rest died at about 4 months. *Stag2<sup>ff/y</sup>* mice did not show differences discernible from WT littermates. Although *Stag2<sup>ff/y</sup>;Nes<sup>Cre</sup>* mice did not present microcephaly, they exhibited frequent hydrocephaly that might contribute to their premature death. The *Stag2<sup>ff/y</sup>;Nes<sup>Cre</sup>* mice displayed normal drinking and feeding behaviors (Figure 1H,I), but showed reduced plasma IGF-1 levels compared to the control mice (Figure 1J). *Stag2<sup>ff/y</sup>;Nes<sup>Cre</sup>* mice showed forepaw and hindlimb clasping (Figure 1K) and limb tremors (Video 1), which were not seen in *Stag2<sup>ff/y</sup>* mice. These data indicate that *Stag2* deficiency in the nervous system causes growth retardation and neurological defects.

### ***Stag2* ablation causes hypomyelination**

Hematoxylin and eosin staining of brain sections of *Stag2<sup>ff/y</sup>;Nes<sup>Cre</sup>* mice did not reveal overt anatomical defects (Figure 2—Figure Supplement 1A). As revealed by immunohistochemistry assays using neuron- or astrocyte-specific antibodies, the differentiation of neurons and astrocytes in *Stag2*-deleted brains were largely normal (Figure 2—Figure Supplement 1B–E). To understand the origins of neurological defects caused by *Stag2* deletion, we analyzed the gene expression changes in *Stag2<sup>ff/y</sup>;Nes<sup>Cre</sup>* mouse brains by RNA-sequencing (RNA-seq) (Figure 2A). Compared with the control groups, 105 and 62 genes were significantly downregulated or

upregulated by more than two folds, respectively, in the *Stag2*-deficient brains. The decreased expression of top differentially expressed genes (DEGs) was confirmed by reverse transcription quantitative PCR (RT-qPCR) (Figure 2B). Among the 105 downregulated DEGs in the brains of *Stag2* cKO mice, 44 were enriched in myelin (Figure 2C) (Thakurela et al., 2016). The Ingenuity Pathway Analysis (IPA) pinpoints cholesterol biosynthesis pathways as the most affected canonical pathways (Figure 2D and Supplementary File 1). We further confirmed that the cholesterol biosynthesis precursors were reduced in *Stag2<sup>f/y</sup>;Nes<sup>Cre</sup>* brains (Figure 2—Figure Supplement 1F).

Myelin is the membrane sheath that wraps around axons to facilitate rapid nerve conduction and maintain metabolic supply (Williamson and Lyons, 2018). Dynamic myelination in the central nervous system (CNS) is critical for proper neurodevelopment, and defective myelination is associated with autoimmune and neurodegenerative diseases (Mathys et al., 2019; Wolf et al., 2021). Cholesterol biosynthesis is essential for normal myelination (Hubler et al., 2018; Saher et al., 2005). Ensheatment of neurons and gliogenesis were among the top enriched biological pathways in downregulated DEGs (Figure 2—Figure Supplement 2). The innate immune response was among the top enriched pathways in the upregulated DEGs. We hypothesized that depletion of STAG2 caused myelination defects in the nervous system.

Indeed, brain sections of *Stag2<sup>f/y</sup>;Nes<sup>Cre</sup>* mice showed greatly reduced luxol fast blue (LFB) staining compared to those of *Stag2<sup>f/y</sup>* and *Nes<sup>Cre</sup>* heterozygous mice (Figure 3A and Figure 3—Figure Supplement 1A). Immunohistochemistry using antibodies against myelin proteins, MBP and PLP1, confirmed that *Stag2* cKO mice had significant defects in myelin fiber formation (Figure 3B–F). In both cerebral cortex and cerebellum, there were fewer and sparser myelin fibers in *Stag2<sup>f/y</sup>;Nes<sup>Cre</sup>* mice, as compared to the *Stag2<sup>f/y</sup>* controls. Axon myelin

ensheathment was further examined using transmission electron microscopy (Figure 3G). *Stag2<sup>f/y</sup>;Nes<sup>Cre</sup>* mice had significantly fewer myelin-wrapped axons at optic nerves. Collectively, these data indicate insufficient myelination in the *Stag2* cKO mice. Myelination predominantly occurs at 3 weeks after birth in the mouse. The timing of premature death of *Stag2* cKO mice is thus consistent with defective myelination as a contributing factor to the lethality.

We examined *Stag1* and *Stag2* expression patterns in wild-type mouse brains by *in situ* hybridization using isotope-labeled RNA probes (Figure 3—Figure Supplement 1B). Both *Stag1* and *Stag2* were expressed at high levels in hippocampus, medial habenula, neocortex, and cerebellum granular layer. Aside from these regions, the *Stag2* transcripts were detected at relatively high levels in subventricular zone, thalamus, fiber tracts, midbrain, and hindbrain regions. *Stag2* is thus ubiquitously expressed in the brain.

## **STAG2 regulates transcription in OLs**

Oligodendrocytes (OLs) are responsible for myelination in the CNS. To examine whether the OL lineage was affected by *Stag2* deletion, we performed single-cell RNA sequencing (scRNA-seq) analysis of *Stag2<sup>f/y</sup>;Nes<sup>Cre</sup>* and *Stag2<sup>f/y</sup>* forebrains. As revealed by clusters in the t-SNE plot, the two genotype groups had similar cellular compositions (Figure 4A,B). All cell clusters were present in *Stag2<sup>f/y</sup>;Nes<sup>Cre</sup>* brains, again indicating generally normal neural cell differentiation. Cell-type identities were discovered with feature gene expression (Figure 4—Figure Supplement 1A). Based on the expression changes of *Stag2* and other cohesin genes in OLs, astrocytes, and neuronal lineages (Figure 4—Figure Supplement 1B–D), it is clear that *Stag2* ablation occurred early in the NPC stage and was maintained in all differentiated cell lineages.

The OL lineage consisted of five clusters: cycling OL progenitors (OPCcyts), OL progenitors (OPCs), newly formed OLs (NFOLs), myelin-forming OLs (mFOLs), and fully matured OLs (MOLs). Quantification of the distributions of these five cell types within the OL lineage revealed a mild reduction in the number of MOLs in *Stag2<sup>f/y</sup>* forebrains (Figure 4C). We noticed that a higher percentage of neurons was recovered in the *Stag2<sup>f/y</sup>;Nes<sup>Cre</sup>* group. Since the bulk RNA-seq results did not show global upregulation of neuron-specific genes, we suspect that neurons in *Stag2<sup>f/y</sup>;Nes<sup>Cre</sup>* had fewer myelin-wrapped axons and were easier to be dissociated and kept alive during our library preparation for scRNA-seq. Thus, from the transcriptome analysis, we did not observe overt defects in most neural cell differentiation in the *Stag2*-deficient forebrain regions.

We then performed trajectory inference and pseudotime analysis of the OL lineage (Figure 4—Figure Supplement 2A,B). Consistent with our cell-type assignment, pseudotime variables indicated continuous differentiation from OPCs to NFOLs, mFOLs, and MOLs (Figure 4—Figure Supplement 2C,D). The re-clustering of single cells in the OL lineage along the pseudotime path revealed that more cells were present in the terminal maturation stages in the *Stag2<sup>f/y</sup>* brains (Figure 4—Figure Supplement 2E,F). Conversely, more cells were retained at the undifferentiated stages in the *Stag2<sup>f/y</sup>;Nes<sup>Cre</sup>* brains. Strikingly, some myelination genes, including *Mal*, were specifically repressed in *Stag2<sup>f/y</sup>;Nes<sup>Cre</sup>* MOLs, with their expression in non-neural cells unaltered (Figures 4D and Figure 4—Figure Supplement 3A). These observations suggest that STAG2 deficiency delays the maturation of OLs and compromises myelination-specific gene expression in mature OLs. Interestingly, compared to *Stag2* and genes encoding other cohesin core subunits, *Stag1* transcripts are less abundant in the OL lineage, except for

cycling OPCs (Figure 4—Figure Supplement 3B,C). The low expression of *Stag1* in mature OLs might make these cells more dependent on *Stag2* for function.

To confirm the transcriptional defects in the OL lineage caused by *Stag2* deletion, we isolated primary OLs at intermediate differentiation stages from *Stag2<sup>f/y</sup>;Nes<sup>Cre</sup>* and *Stag2<sup>f/y</sup>* forebrains with antibody-conjugated magnetic beads and conducted bulk RNA-seq analysis (Figure 4E). For both genotypes, the marker genes for NFOL and mFOLs were highly expressed in the isolated primary OLs (Figure 4—Figure Supplement 4A), suggesting that they mainly contained these two cell types. In *Stag2*-deleted OLs, 271 and 292 genes were downregulated or upregulated by more than two folds, respectively (Figure 4F and Supplementary File 2). Intriguingly, the downregulated genes were generally highly expressed in WT cells, whereas the upregulated genes had low expression levels in WT cells (Figure 4—Figure Supplement 4B–D). The top pathways enriched in the downregulated DEGs included the cholesterol and small molecule biosynthetic pathways and oligodendrocyte differentiation (Figure 4G and Figure 4—Figure Supplement 5). Cilium organization and assembly are the top enriched pathways in the upregulated DEGs (Figure 4—Figure Supplement 6). Among the 105 downregulated DEGs identified by RNA-seq analysis of the whole brain of *Stag2*-deficient mice, 42 were also differentially expressed in primary oligodendrocytes (Figure 4H). The cholesterol biosynthetic pathways were recognized as the major altered pathways (Figure 4—Figure Supplement 4E). Thus, defective cholesterol biosynthesis and oligodendrocyte differentiation likely underly hypomyelination and neurological defects in *Stag2* cKO mice.

We performed chromatin immunoprecipitation sequencing (ChIP-seq) experiments to examine the enrichment of the active transcription mark H3K27ac in *Stag2<sup>f/y</sup>* and *Stag2<sup>f/y</sup>;Nes<sup>Cre</sup>* OLs and found that *Stag2* loss did not appreciably affect H3K27Ac enrichment at transcription

start sites (TSS) (Figure 5A,B). Consistent with our RNA-seq results, the upregulated genes had much lower H3K27ac enrichment near their TSS, indicating that they were less active. We then checked the genomic distribution of STAG2 by ChIP-seq. Among other genomic loci, STAG2 was enriched at TSS of stable and downregulated genes, including genes in the cholesterol biosynthesis and myelination pathways (Figure 5C,D, Figure 5—Figure Supplement 1, and Supplementary File 2). Among the 271 downregulated DEGs, there were 210 genes (77%) with STAG2 enrichment near the transcriptional start site ( $TSS \pm 2$  kb). Thus, STAG2 occupied the promoter regions of many downregulated DEGs in oligodendrocytes. It was enriched at the TSS of upregulated genes to a lesser extent, with only 117 of the 292 (40%) upregulated DEGs exhibiting STAG2 ChIP-seq peaks at their  $TSS \pm 2$  kb regions. *Stag2* loss might have indirectly affected the expression of these less active genes.

#### ***Stag2* deletion does not alter compartments or TADs in OLs**

To investigate whether chromosome conformation was altered by *Stag2* deletion and whether that caused transcription dysregulation, we performed high-dimensional chromosome conformational capture (Hi-C) analysis of primary OLs isolated from *Stag2<sup>f/y</sup>* and *Stag2<sup>f/y</sup>;Nes<sup>Cre</sup>* mice in biological replicates (Figure 6 and Figure 6—Figure Supplement 1). We observed few compartment switching events in *Stag2*-deleted cells (Figure 6A–C). Virtually all genomic regions in *Stag2*-deleted cells were kept in their original compartment categories (AA or BB) (Figure 6C). Only a very small number of genomic regions switched compartments (AB or BA). Consistent with the RNA-seq data, analysis of average gene expression changes of DEGs in these genomic regions revealed that more genes located in the transcriptionally active A compartment (AA) were repressed in *Stag2*-deleted cells and more genes in the transcriptionally

silent B compartment (BB) were upregulated (Figure 6D and Figure 6—Figure Supplement 1C). Genes that switched from the A compartment to the B compartment were not more repressed compared to those that remained in the A compartment. Likewise, compared to genes that stayed in the B compartment, genes located in chromatin regions that switched from compartment B to A were not significantly activated. Acute depletion of all forms of cohesin eliminates TAD formation (Wutz et al., 2017). In contrast, deletion of *Stag2* had minimal impact on TAD formation in oligodendrocytes (Figure 6E–G and Figure 6—Figure Supplement 1D), suggesting that STAG1-cohesin compensates for the loss of STAG2-cohesin in spatial organization of chromatin at larger than megabase scales. Therefore, our analyses did not uncover evidence for compartment switching and TAD alterations being the underlying cause for the observed gene expression changes in STAG2-deficient OLs.

#### **Promoter-anchored loops were reduced in *Stag2*-deleted OLs**

While TAD boundaries are largely conserved among species and cell types, chromatin interactions within each TAD are more flexible and variable in cells undergoing differentiation, tumorigenesis, and reprogramming (Dixon et al., 2015; Dixon et al., 2012). Among the intra-TAD chromatin interactions, the enhancer-promoter loops are particularly important for transcription and are often cell-type specific. We examined whether chromatin loops in OLs were affected by *Stag2* loss. Compared to *Stag2<sup>f/y</sup>* OLs, *Stag2<sup>f/y</sup>;Nes<sup>Cre</sup>* OLs had significantly fewer loops across almost all genomic distances (Figure 7A,B and Figure 7—Figure Supplement 1). The common and genotype-specific loops are reproducible in each replicate. Loops specific to *Stag2<sup>f/y</sup>;Nes<sup>Cre</sup>* OLs, which were likely mediated by STAG1-cohesin, were longer than STAG2-dependent *Stag2<sup>f/y</sup>*-specific loops. When genomic distances exceeded 0.25 Mb, the

loops from *Stag2<sup>f/y</sup>;Nes<sup>Cre</sup>* cells gradually gained higher scores over loops from *Stag2<sup>f/y</sup>* cells (Figure 7C). Therefore, STAG1-cohesin cannot completely compensate for STAG2-cohesin during loop formation. STAG1-cohesin-mediated loops are relatively longer than STAG2-cohesin-mediated loops, consistent with published findings in HeLa cells (Wutz et al., 2020).

We then tested whether the loop number decrease in *Stag2*-deficient cells could be a cause for transcriptional changes. When examining the local Hi-C maps, we noticed that loops anchored at gene promoters, including those of downregulated genes, were reduced in *Stag2<sup>f/y</sup>;Nes<sup>Cre</sup>* oligodendrocytes (Figure 7D, Figure 7—Figure Supplement 2A–C, and Supplementary File 2). The effects were again reproducible in each replicate (Figure—Figure Supplement 2D). Promoter-anchored loops (P-loops) can potentially be promoter-promoter links, promoter-enhancer links, and gene loops. The total number of P-loops was proportionally decreased in *Stag2<sup>f/y</sup>;Nes<sup>Cre</sup>* cells (Figure 7—Figure Supplement 3A). Moreover, the loops anchored at the downregulated genes were stronger than those at upregulated and stable genes (Figure 7—Figure Supplement 3B). We then compared P-loops associated with DEGs using pileup analysis of local contact maps. Loop enrichment at promoters of downregulated genes was reduced in *Stag2<sup>f/y</sup>;Nes<sup>Cre</sup>* cells to a greater extent than that at promoters of upregulated and stable genes (Figure 7E). Among the 162 downregulated DEGs with reduced promoter-anchored loops in the *Stag2*-depleted cells, 137 genes (85%) had STAG2 peaks in their promoter regions (TSS  $\pm$  2kb). The loops anchored at down-regulated genes with STAG2 binding had significantly higher loop scores, compared to those with no STAG2 binding (Figure 7—Figure Supplement 3C,D). This difference was still observed in *Stag2*-deleted cells, suggesting that the stronger looping at these gene promoters might be maintained by STAG1-cohesin or other factors in these cells. By contrast, the loops anchored at upregulated genes with STAG2 binding

279 had lower loop scores. These differences became insignificant in the *Stag2*-deleted cells. The  
280 loop scores of loops anchored at stable genes were not affected by STAG2 occupancy. Taken  
281 together, our results suggest that *Stag2* loss diminishes the number of, but not the strength, of  
282 short chromosome loops, including promoter-anchored loops. Highly expressed genes might be  
283 more reliant on these loops for transcription and are preferentially downregulated by *Stag2* loss.

284 We also performed pileup analysis of local chromatin regions flanking transcription start  
285 sites (TSS) (Figure 7F). Strikingly, we observed a clear stripe that extended from the TSS of  
286 downregulated gene only in the direction of transcription. The formation of promoter-anchored  
287 stripes (P-stripes) on aggregated plots is consistent with one-sided loop extrusion from the  
288 promoter to the gene body. The P-stripe was still present in *Stag2*<sup>f/y</sup>;*Nes*<sup>Cre</sup> cells, suggesting that  
289 STAG1 could compensate for the loss of STAG2 and mediate its formation (Figure 7F and  
290 Figure 7—Figure Supplement 3E).

## Discussion

Cohesin is critical for the three-dimensional (3D) organization of the genome by extruding chromosome loops. Acute depletion of cohesin abolishes chromosome loops and TADs, but has moderate effects on transcription. The two forms of cohesin in vertebrate somatic cells, namely STAG1-cohesin and STAG2-cohesin, have largely redundant functions in supporting sister-chromatid cohesion and cell viability, but they have non-redundant functions during development. In this study, we have established a myelination-promoting function of STAG2 in the central nervous system (CNS) in the mouse. We further provide evidence linking hypomyelination caused by STAG2 loss to reduced promoter-anchored loops at myelination genes in oligodendrocytes.

### Myelination functions of STAG2 and implications for cohesinopathy

Selective ablation of *Stag2* in the nervous system in the mouse causes growth retardation, neurological defects, and premature death. STAG2 loss delays the maturation of oligodendrocytes and reduces the expression of highly active myelin and cholesterol biosynthesis genes in oligodendrocytes, resulting in hypomyelination in the CNS. Hypomyelination disorders in humans and mice are known to produce abnormal neurological behaviors similar to those seen in our *Stag2* cKO mice, suggesting that hypomyelination is a major underlying cause for the phenotypes in *Stag2* cKO mice. The growth retardation in these mice can be explained by insufficient secretion of growth hormones, which may be a consequence of defective neuronal signaling.

Mutations of cohesin subunits and regulators, including STAG2, cause the Cornelia de Lange syndrome (CdLS) and other similar developmental diseases, collectively termed

cohesinopathy. CdLS patients exhibit short stature and developmental defects in multiple tissues and organs, including the brain. Although STAG2 mutations are implicated in human cohesinopathy, these mutations are rare and hypomorphic (Soardi et al., 2017). The cohesin loader NIPBL is the most frequently mutated cohesin regulator in cohesinopathy (Mannini et al., 2013). NIPBL deficiency is expected to affect the functions of both STAG1- and STAG2-cohesin. It is possible that the partial loss of STAG2-cohesin function leads to subtle myelination defects in patients with cohesinopathy. Indeed, lack of myelination in certain brain regions of CdLS patients has been reported (Avagliano et al., 2017; Vuilleumier et al., 2002). As myelination of the CNS mostly occurs after birth and during childhood, strategies aimed at enhancing myelination might help to alleviate certain disease phenotypes and symptoms.

### **Mechanisms by which STAG2 promotes myelination**

STAG2 promotes oligodendrocyte maturation and the expression of myelination genes in mature oligodendrocytes. Because STAG2 does not have an established cohesin-independent function, it most likely activates the myelination-promoting transcriptional program as a core component of cohesin. Consistent with previous reports (Rao et al., 2017), loss of STAG2-cohesin in oligodendrocytes does not affect genome compartmentalization, but reduces the number of relatively short chromosome loops, including promoter-anchored loops. Promoter-anchored loops at downregulated genes are reduced to a greater extent than those at stable and upregulated genes. These findings suggest that STAG2-cohesin promotes the myelination transcriptional program by forming promoter-anchored loops.

Pileup analysis of Hi-C maps reveals the formation of asymmetric promoter-anchored stripes in the direction of transcription at downregulated genes, indicative of active loading of

cohesin at transcription start sites followed by one-sided loop extrusion from the promoter to the gene body. The stripes are, however, not reduced in STAG2-deficient cells. Because both forms of cohesin are capable of loop extrusion, it is possible that STAG1-cohesin can compensate for the loss of STAG2-cohesin in loop extrusion. It remains to be tested whether the intrinsic kinetics and processivity of loop extrusion mediated by the two forms of cohesin are differentially regulated by cellular factors or posttranslational modifications and whether these differences contribute to their non-redundant roles in transcription regulation.

We envision three possibilities that may account for why oligodendrocytes, but not other cell types, are more severely affected by *Stag2* loss in the CNS. First, STAG2-cohesin may be more abundant than STAG1-cohesin in post-mitotic OLs, making them more dependent on STAG2 for proper functions. Second, STAG1-cohesin preferentially localizes to CTCF-enriched TAD boundaries whereas STAG2-cohesin is more enriched at enhancers lacking CTCF (Kojic et al., 2018). Enhancers are critical for cell-type-specific gene transcriptional programs. To cooperate with the axonal growth during postnatal neurodevelopment, enhancer-enriched transcription factors induce timely and robust gene expression in oligodendrocytes for proper myelination (Mitew et al., 2014). The high-demand for enhancer function may render the transcription of myelination genes more reliant on STAG2-cohesin. Finally, the C-terminal regions of STAG1 and STAG2 are divergent in sequence and may bind to different interacting proteins and be subjected to differential regulation. STAG2 may interact with oligodendrocyte-specific transcription factors and be preferentially recruited to myelination genes. It will be interesting to investigate the interactomes of STAG1 and STAG2 in oligodendrocytes using mass spectrometry.

## **STAG2-mediated chromosome looping and transcription**

The mechanisms by which STAG2-dependent chromosome looping facilitates transcription are unclear at present. We propose several models that are not mutually exclusive (Figure 8). First, by forming promoter-enhancer loops, STAG2-cohesin brings the mediator complex and other enhancer-binding factors to the spatial proximity of the general transcriptional machinery at the promoter, thereby enhancing RNA polymerase II recruitment and transcription initiation. The existence of P stripes at STAG2-dependent genes in the Hi-C maps suggests that STAG2-mediated promoter-enhancer loops may involve enhancers located in the gene body. Second, loop extrusion by STAG2-cohesin may promote transcription elongation by regulating transcription-coupled pre-mRNA processing. For example, STAG2 has been shown to interact with RNA-DNA hybrid structures termed R-loops *in vitro* and in cells (Pan et al., 2020; Porter et al., 2021). R-loops formed between the nascent pre-mRNA and the DNA template impede transcription elongation and need to be suppressed (Moore and Proudfoot, 2009). When traveling with the transcription machinery on DNA, STAG2-cohesin might directly suppress R-loop formation or recruit other factors, such as the spliceosome, for co-transcriptional pre-mRNA processing and R-loop resolution. Third, STAG2-cohesin may establish promoter-terminator gene loops to recycle the RNA polymerase II that has finished one cycle of transcription back to the transcription start site for another round of transcription. Future experiments using high-resolution Hi-C methods in oligodendrocytes and ChIP-seq experiments with additional enhancer- and promoter-specific histone marks will allow us to better define the nature of STAG2-dependent promoter-anchored loops and stripes. It will also be interesting to examine whether *Stag2* deletion causes the accumulation of R-loops in downregulated genes and the incomplete splicing of their pre-mRNAs.

384

385

## CONCLUSION

We have discovered a requirement for the cohesin subunit STAG2 in the myelination of the central nervous system in mammals. Our findings implicate hypomyelination as a contributing factor to certain phenotypes of cohesinopathy, including growth retardation and neurological disorders. We provide evidence to suggest that STAG2 promotes the myelination transcriptional program in oligodendrocytes through the formation of promoter-anchored loops. Our study establishes oligodendrocytes as a physiologically relevant cell system for dissecting the cellular functions and regulatory mechanisms of cohesin-mediated chromosome folding and genome organization.

## Materials and methods

**Generation of mouse lines and mouse husbandry.** All animals were handled in accordance with institutional guidelines of the Institutional Animal Care and Use Committee (IACUC; AAALAC unit number 000673) of University of Texas (UT) Southwestern Medical Center under the animal protocol number (APN) 102335. The *Stag2* locus was targeted by inserting one neo cassette and two loxP sites flanking exon 8 via homologous recombination in the mouse embryonic stem (ES) cells. G418-selected positive ES clones were screened for successful targeting by nested PCR tests on both 5' and 3' integration sites of loxP. Four confirmed ES clones were then microinjected into mouse blastocysts. The chimeras were bred to the R26FLP mouse line for the removal of the neo cassette. *Stag2*<sup>f/+</sup> mice with the 129/B6 background were crossed with *Stag2*<sup>f/y</sup> or wildtype C57BL/6J mice and maintained on this background. For the generation of the inducible system of *Stag2*<sup>f/y</sup>;*Rosa26*<sup>CreERT2</sup> mice, *Stag2*<sup>f/f</sup> mice were bred to the mouse strain that contains two alleles of the conditional Cre-ER<sup>T2</sup> cassette (B6.129-Gt(ROSA)26Sortm1(cre/ERT2)Tyj/J, JAX stock #008463) (Ventura et al., 2007). For the generation of the nervous system-specific *Stag2*<sup>f/y</sup>;*Nes*<sup>Cre</sup> mice, the *Stag2*<sup>f/f</sup> mice were crossed with the transgenic mice carrying one allele of Cre recombinase driven by the rat nestin promoter and enhancer (Tg(Nes-cre)1Kln, JAX stock #003771) (Giusti et al., 2014; Tronche et al., 1999).

Whole-body knockout mice were generated by CRISPR-Cas9 gene editing technology. Briefly, a pair of guide RNAs (sgRNA; sequences listed in the Key Resource Table) targeting genomic sequence flanking exon 8 of the *Stag2* locus were tested for cutting efficiency in cell culture, transcribed *in vitro*, purified, checked for integrity, and microinjected into B6C3F1 mouse zygotes along with the *Cas9* mRNA (5-methylcytidine, pseudouridine, TriLink). 20 ng/μl of *Cas9* mRNA and 10 or 20 μg/μl each of sgRNA were used. The injected embryos were

transferred to the surrogate mother on the same day. Mosaic F<sub>0</sub> founders carrying the *Stag2*<sup>null</sup> allele were identified by PCR genotyping. The reduction of the STAG2 protein was confirmed by Western blotting in multiple tissues. The F<sub>0</sub> founders were crossed with wildtype C57BL/6J mice to generate the *Stag2*<sup>+/-</sup> F<sub>1</sub>. The mutations in F<sub>1</sub> were identified by Sanger Sequencing. Two mouse lines carrying genomic deletions between the Cas9 cleavage sites were chosen for the generation of *Stag2*<sup>null</sup> mouse embryos.

All mice were housed in the antigen-free barrier facility with 12 hr light/dark cycles (6 AM on and 6 PM off). Mice were fed a standard rodent chow (2016 Teklad Global 16% protein rodent diet, Harlan Laboratories).

**Immunoblotting.** The C-terminal fragment of human STAG2 protein was expressed and purified from *Escherichia coli* and used as the antigen to generate rabbit polyclonal antibodies against STAG2 at YenZym. Other antibodies were purchased from the following commercial sources: anti-SMC1 (Bethyl Laboratories, A300-055A), anti-SMC3 (Bethyl Laboratories, A300-060A), anti-RAD21 (Bethyl Laboratories, A300-080A), anti-SA1 (Bethyl Laboratories, A302-579A), anti-SA2 (Bethyl Laboratories, A302-581A), anti- $\alpha$ -TUBULIN (Sigma-Aldrich, DM1A), anti-MBP (Abcam, ab7349), anti-PLP1 (Abcam, ab28486), and anti-H3K27ac (Abcam, ab4729).

For immunoblotting, brain hemispheres were homogenized in a Precellys tissue homogenizer (Bertin Instruments) with the lysis buffer [20 mM Tris-HCl (pH 7.7), 137 mM NaCl, 2 mM EDTA, 10% (v/v) glycerol, 1% (v/v) TritonX-100, 0.5 mM dithiothreitol, 1 mM PMSF, 1 mM Na<sub>3</sub>VO<sub>4</sub>, 10 mM  $\beta$ -glycerophosphate, 5 mM NaF and protease inhibitors (Roche)]. Homogenized brain tissues were lysed on ice for 1 hr. The lysate was then subjected to centrifugation at 20,817 g at 4°C for 20 min and further cleared by filtering through a 0.45  $\mu$ m

filter. The cleared lysate was analyzed by SDS-PAGE and transferred to membranes, which was then incubated with the appropriate primary and secondary antibodies. The blots were imaged with the Odyssey Infrared Imaging System (LI-COR).

**Tissue histology and immunohistochemistry.** Mouse brains were fixed in 10% neutral buffered formalin solution for 48 hr followed by paraffin embedding and coronal or sagittal sectioning at 5  $\mu$ m. Hematoxylin and eosin (H&E) staining and Luxol fast blue staining were performed by the Molecular Pathology Core at UT Southwestern Medical Center. Investigators were blinded to the genotype. Images were acquired with the DM2000 microscope (Leica) at 1.25X resolution.

Immunohistochemistry was performed as previously described (Choi et al., 2016). Briefly, deparaffinized sections were fixed with 4% paraformaldehyde, subjected to antigen retrieval by boiling with 10 mM sodium citrate (pH 6.0), and then incubated with the indicated antibodies at 1:100 dilution. The slides were scanned with an Axioscan.Z1 microscope (Zeiss) at 40X resolution at the Whole Brain Microscopy Facility at UT Southwestern Medical Center. Images were processed and quantified with Image J. For the myelinated fiber length measurement and coherency analysis, coronal sections of the brain cortex stained with the anti-MBP antibody were processed as previously described (van Tilborg et al., 2017). The myelinated axial thinning and fiber length measurement were performed by the plugin DiameterJ. The coherency analysis of myelinated axons was performed with the plugin OrientationJ.

**Isolation of primary oligodendrocytes.** The immunomagnetic isolation of oligodendrocytes from *Stag2<sup>f/y</sup>* and *Stag2<sup>f/y</sup>;Nes<sup>Cre</sup>* P12-P14 pups was conducted using anti-O4 microbeads (Miltenyi Biotec) according to a published protocol (Flores-Obando et al., 2018). Briefly, brain cortices were dissected, pooled, minced into 1mm<sup>3</sup> cubes, and incubated with the Papain dissociation solution (Neurobasal Medium with 1% Penicillin-Streptomycin, 1% L-glutamine, 2% B27 supplement, 20-30 U/ml of Papain and 2500 U DNase I) in a 37°C, 5% CO<sub>2</sub> incubator for more than 20 min. The enzymatic digestion was inactivated by the addition of 1 ml of fetal bovine serum (FBS). Gentle trituration by 10-ml, 5-ml and 1 ml pipettes was applied to break up cell clumps. Cells were collected by centrifugation (200 x g, 10 min), washed first with serum-containing medium (Neurobasal Medium with 1% Penicillin-Streptomycin, 1% L-glutamine, 2% B27 supplement and 10% FBS), and then with the magnetic cell sorting (MCS) buffer (PBS, pH 7.2, with 0.5% bovine serum albumin (BSA), 0.5 mM EDTA, 5 µg/ml insulin and 1 g/l glucose). The cell pellet was resuspended in the MCS buffer and incubated with anti-O4 microbeads at 10 µl/10<sup>7</sup> cells at 4°C for 15 min followed by 1x wash with the MCS buffer. The O4<sup>+</sup> immature oligodendrocytes were sorted through the magnetic LS columns according to the manufacturer's instruction. Freshly prepared oligodendrocytes were directly used or fixed for subsequent analysis.

**Metabolic cage analysis.** Mice were singly housed in shoebox-sized cages with a five-day acclimation period followed with a four-day recording period. Recorded parameters were analyzed by the TSE system and normalized to body weight. The experiments were conducted by the core personnel under the core protocol at the Metabolic Phenotyping Core at UT Southwestern Medical Center. Investigators were blinded to the genotype.

**Growth hormone and IGF-1 detection.** Blood samples were collected from facial bleeding without fasting. Plasma growth hormone levels were determined with the rat/mouse growth hormone ELISA kit (EMD Milipore, EZRMGH-45K). Plasma IGF-1 concentrations were measured using the mouse/rat IGF1 Quantikine ELISA kit (R&D Systems).

**Sterol and oxysterol composition analysis.** Brain hemispheres were pre-weighed and snap-frozen for extraction and measurement by mass spectrometry. The sterol extraction and quantitative analysis were conducted at the Center of Human Nutrition at UT Southwestern Medical Center as described previously (McDonald et al., 2012).

**Electron microscopy.** *Stag2<sup>f/y</sup>* and *Stag2<sup>f/y</sup>;Nes<sup>Cre</sup>* P18 pups were transcardially perfused with 4% paraformaldehyde, 1% glutaraldehyde in 0.1 M sodium cacodylate buffer (pH 7.4). Tissues were dissected and fixed with 2.5% (v/v) glutaraldehyde in 0.1 M sodium cacodylate buffer (pH 7.4) for at least two hours. After three rinses with the 0.1 M sodium cacodylate buffer, optic nerve samples were embedded in 3% agarose and sliced into small blocks. All samples were again rinsed with the 0.1M sodium cacodylate buffer three times and post-fixed with 1% osmium tetroxide and 0.8 % potassium ferricyanide in the 0.1 M sodium cacodylate buffer for three hours at room temperature. Blocks were rinsed with water and *en bloc* stained with 4% uranyl acetate in 50% ethanol for two hours. Samples were dehydrated with increasing concentrations of ethanol, transitioned into propylene oxide, infiltrated with Embed-812 resin, and polymerized in a 60°C oven overnight. Blocks were sectioned with a diamond knife (Diatome) on a Leica Ultracut 7 ultramicrotome (Leica Microsystems) and collected onto copper grids, post-stained

with 2% aqueous uranyl acetate and lead citrate. Images were acquired on a Tecnai G2 Spirit transmission electron microscope (Thermo Fischer) equipped with a LaB6 source using a voltage of 120 kV. Tissue processing, sectioning, and staining were completed by the Electron Microscopy Core at UT Southwestern Medical Center.

**RNA-seq library preparation and sequencing.** Total RNA was extracted from brain hemispheres or isolated oligodendrocytes with Trizol. RNA integrity was determined by the Agilent BioAnalyzer 2100. TruSeq Stranded mRNA library prep kit (Illumina) was used to generate the mRNA libraries. The libraries were analyzed by the Bioanalyzer and multiplexed and sequenced using the NextSeq 500 high output kit (400M reads) for the brain libraries or NextSeq 500 mid output kit (130M reads) for the isolated oligodendrocytes libraries at the Next Generation Sequencing Core at UT Southwestern Medical Center.

**Differential expression and pathway analysis.** Raw data from the sequencer were de-multiplexed and converted to fastq files using bcl2fastq (v2.17, Illumina). The fastq files were checked for quality using fastqc (v0.11.2) (Andrews, 2010) and fastq\_screen (v0.4.4) (Wingett, 2011). Fastq files were mapped to the mm10 mouse reference genome (from iGenomes) using STAR (Dobin et al., 2013). Read counts were then generated using featureCounts (Liao et al., 2014). TMM normalization and differential expression analysis were performed using edgeR (Robinson et al., 2010). Pathway analysis was performed with the Ingenuity pathway analysis (IPA) software. Genes with more than 1.5-fold change and FDR < 0.01 were included in the brain RNA-seq pathway analysis. Genes with more than 2-fold change and FDR < 0.05 were used for the pathway analysis of the RNA-seq data from oligodendrocytes.

**RT-qPCR analysis.** Single-stranded cDNAs were converted from 2 µg of total RNA extracted from mouse brains with the high-capacity cDNA reverse transcription kit (Applied Biosystems). Quantitative-PCR was conducted to determine transcript levels using gene-specific TaqMan probes (Applied Biosystems).

**Single-cell RNA-seq.** Single-cell suspension was prepared from forebrains of P13 *Stag2<sup>f/y</sup>* or *Stag2<sup>f/y</sup>;Nes<sup>Cre</sup>* pups using the Papain Dissociation System (Worthington Biochemical, LK003150) according to the manufacturer's instructions. Biological duplicates were made for each genotype. Single-cell RNA-seq libraries were generated with the Chromium Single Cell 3' GEM, Library & Gel Bead Kit v3 (10x Genomics) according to the manufacturer's guidelines. Cell density and viability were checked by the TC-20 Cell Counter (Bio-Rad). Cells were then loaded onto Chip B in the Chromium Controller (10x Genomics). 10,000 cells were targeted for each sample. The libraries were analyzed by the Bioanalyzer (Agilent) and pair-end sequenced in two flowcells of the NextSeq 500 High Output (400M) run. The sequencing was performed at the Next Generation Sequencing Core at UT Southwestern Medical Center.

Data de-multiplexing and alignment was performed using the Cell Ranger pipeline (<https://support.10xgenomics.com/single-cell-gene-expression/software/pipelines/latest/using/mkfastq>) (10x Genomics). The raw features, barcodes, and matrixes were used as input for further analysis using the R package Seurat3 (Butler et al., 2018; Stuart et al., 2019) (<https://satijalab.org/seurat/>). Cells were filtered by the following criteria: nFeature\_RNA (200-9500) and percent.mt < 10. After filtering, a total of 5,834 cells in *Stag2<sup>f/y</sup>#1*, 4,699 cells in *Stag2<sup>f/y</sup>#2*, 9,050 cells in *Stag2<sup>f/y</sup>;Nes<sup>Cre</sup>#1*, and 3,073 cells in *Stag2<sup>f/y</sup>;Nes<sup>Cre</sup>#2* were used for

downstream analysis. 2,000 variable features were found from each normalized dataset. All datasets were then integrated using identified anchors (dims = 1:30). Standard scaling and principal component analysis (PCA), clustering (resolution = 0.5), and tSNE reduction (dims = 1:30) were performed on the integrated dataset. Cluster biomarkers were identified, and top features were examined. Clusters were then manually assigned to distinct cell type identities with knowledge from previous studies (Cahoy et al., 2008; Dulken et al., 2019; Marques et al., 2018; Marques et al., 2016; Marton et al., 2019; Saunders et al., 2018; Zeisel et al., 2018; Zywitza et al., 2018) (<http://www.brainrnaseq.org/>) (<http://dropviz.org/>). Clusters with the same cell type identities were merged. 5 clusters of oligodendrocyte lineage [cycling oligodendrocyte progenitors (OPCcycs), oligodendrocyte progenitors (OPCs), newly formed oligodendrocytes (NFOLs), myelin-forming oligodendrocytes (mFOLs) and fully matured oligodendrocytes (MFOLs)] were identified and selected for indicated gene expression comparison and plotting using Vlnplot or FeaturePlot functions. The trajectory analysis was performed using Monocle3 (Cao et al., 2019) in the oligodendrocyte cell population. Gene density plot over pseudotime was generated as previously described (Luecken and Theis, 2019).

**ChIP-seq.** Chromatin immunoprecipitation (ChIP) was performed as previously described (Liu et al., 2017). Briefly, isolated oligodendrocytes were fixed with 1% formaldehyde and fragmented with a sonicator (Branson 450). The fragmented chromatin was incubated with antibodies overnight at 4°C. Dynabeads Protein A (Thermo Fisher Scientific) was used for the immunoprecipitation. Libraries were generated by the Next Gen DNA Library Kit (Active Motif) with the Next Gen Indexing Kit (Active Motif) for STAG2 ChIP-seq or the KAPA HyperPrep Kits (KAPA Systems) for histone ChIP-seq. The libraries were analyzed by the

Bioanalyzer and pool-sequenced with the NextSeq 500 mid output (130M) kit. After mapping reads to the mouse genome (mm10) by bowtie2 (v2.2.3) (Langmead and Salzberg, 2012) with the parameter “–sensitive”, we performed filtering by removing alignments with mapping quality less than 10 and then removing duplicate reads identified by Picard MarkDuplicates (v1.127). For STAG2 ChIP-seq, Picard MarkDuplicate was used to remove duplicates together with options to use molecular identifiers (MIDs) information in the reads. Enriched regions (peaks) were identified using MACS2 (v2.0.10) (Zhang et al., 2008), with a q-value cut-off of 0.05 for peaks. Peak regions were annotated by HOMER(Ross-Innes et al., 2012).

**Hi-C library generation, sequencing, and analysis.** Hi-C was performed at the Genome Technology Center at NYU Langone Health from 3.5-4.0 µg of DNA isolated from cells cross-linked with 2% formaldehyde at room temperature for 10 minutes. Experiments were performed in duplicates following the instructions from the Arima Hi-C kit (Arima Genomics, San Diego, CA). Subsequently, Illumina-compatible sequencing libraries were prepared by using a modified version of the KAPA HyperPrep library kit (KAPA BioSystems, Willmington, MA). Quality check steps were performed to assess the fraction of proximally ligated DNA labeled with biotin, and the optimal number of PCR reactions needed to make libraries. The libraries were loaded into an Illumina flowcell (Illumina, San Diego, CA) on a NovaSeq 6000 instrument for paired-end 50 reads.

Hi-C analysis was performed using the HiC-Bench pipeline (Lazaris et al., 2017; Tsigirgos et al., 2012) (<https://github.com/NYU-BFX/hic-bench>) and HiC-Pro v3.1.0 (Servant et al., 2015). The read pairs were aligned and filtered with the following parameters: Genome-build=mm10; –very-sensitive-local –local; mapq=20; –min-dist 25000 –max-offset 500. The Juicer “pre” tool

(Durand et al., 2016) (<https://github.com/aidenlab/juicer>) was used to generate the .hic file with default parameters. Sample duplicates were combined. The compartment analysis was done using the HOMER tool (Heinz et al., 2010) (<http://homer.ucsd.edu/homer/index.html>) with 100 kb bins. H3K27ac ChIP-seq data were used to assign A/B compartments. Eigenvector-1 bins were considered shifted (AB and BA) when the bin sign changed and the delta value was greater than 1.5. Topologically associated domains (TAD) and boundaries were identified at 40 kb resolution with the HiCRatio method with the follow parameters: `--min-lambda=0.0 --max-lambda=1.0 --n-lambda=6 --gamma=0 --distance=500kb --fdr=0.1`. TADs were also identified using the Juicer tools (v1.22.01) arrowhead at 10 kb and 25 kb resolution. Aggregate TAD analysis was performed on TAD boundaries by coolpup.py (Flyamer et al., 2020) or GENOVA (van der Weide et al., 2021). The .hic files were converted to .cool format for visualization and plotting with pyGenomeTracks (Lopez-Delisle et al., 2020) at 5 kb resolution.

**Intra-TAD activity analysis.** Common TADs were defined as their boundaries close as  $\pm 120$  kb across the two samples of genotypes. A paired two-sided t-test was performed on each single interaction bin within each common TAD between the two samples. The difference between the average scores of all interaction intensities within the TADs were calculated as the mean intra-TAD activity change. A multiple testing correction by calculating the false-discovery rate per common TAD was also computed. The analysis was performed on the IC-normalized matrices that were re-normalized by CPM or distance. A threshold of  $\log_{2}FC = 0.2$ ;  $FDR = 0.1$  and mean-difference = 0.1 was applied to the analysis.

**Loop analysis and RNA-seq integration.** The loops were classified into group-specific loops

and common loops by using the significance cutoffs provided by Fit-HiC (Ay et al., 2014). A qvalue cutoff of 0.01 was used to identify significant loops in both groups. A loop is considered “group-specific” if it is only present in one group with a  $qval < 0.01$  and not present in the other group with cutoff of  $qval < 0.1$ . Loop anchors were annotated with the gene promoter information (promoter defined as  $\pm 2$  kb from the transcription start site (TSS)). The genes were classified into “down” and “up” regulated genes using an FDR cutoff of 0.05, logFC cutoff of  $\pm 0.58$  and  $\log CPM > 0$ . “stable” or less changed genes are defined as  $\log FC < 0.38$ , and  $\log CPM > 0$ . Random 1,000 genes were chosen for analysis and plotting. The active genes ( $\log CPM > 0$ ) were also grouped in “high”, “mid” and “low” expression groups by separating the genes in three quantiles according to the logCPM values. For the loop enrichment scores, normalized contact scores were computed using Fit-HiC at 10 kb resolution and bias corrected. Pileup analysis was performed with coolpup.py (Flyamer et al., 2020) with the KR method to balance the weight and random shift controls for distance normalization at 5 kb or using GENOVA.

#### **Data availability**

The RNA-seq, scRNA-seq, ChIP-seq, and Hi-C datasets generated and analyzed during the current study are available in the GEO repository, with the accession number GSE186894.

#### **Additional files**

- Video 1. Neurological defects of brain-specific *Stag2* KO mice.
- Supplementary file 1. List of enriched pathways of differentially expressed genes between WT and *Stag2* KO mouse brains as revealed by IPA analysis.

- Supplementary file 2. List of differentially expressed genes between WT and *Stag2* KO oligodendrocytes, with the status of STAG2 binding at their promoters and the numbers of promoter-anchored loops indicated.
- Transport reporting form

## Acknowledgements

We thank Sung Jun Bae for taking the mouse photos and John Shelton for help with histology and *in situ* hybridization. We are grateful to Jeffrey McDonald for the sterol composition analysis, Richard Lu and Lu Sun for providing reagents and advice for the isolation of oligodendrocytes, and Applied Bioinformatics Laboratories at NYU Langone Health for the Hi-C analysis. We also thank the Yu lab members for helpful discussions and for reading the manuscript critically. This study was supported by the National Natural Science Foundation of China (Project 32130053), the U.S. National Institutes of Health (1R01GM124096), the Cancer Prevention and Research Institute of Texas (CPRIT) (RP160667-P2), and the Welch foundation (I-1441).

## Declaration of interests

The authors declare no competing interests.

## References

- Andrews, S. (2010). FastQC: a quality control tool for high throughput sequence data.
- Avagliano, L., Grazioli, P., Mariani, M., Bulfamante, G.P., Selicorni, A., and Massa, V. (2017). Integrating molecular and structural findings: Wnt as a possible actor in shaping cognitive impairment in Cornelia de Lange syndrome. *Orphanet J. Rare Dis.* *12*, 174.
- Ay, F., Bailey, T.L., and Noble, W.S. (2014). Statistical confidence estimation for Hi-C data reveals regulatory chromatin contacts. *Genome Res* *24*, 999-1011.
- Butler, A., Hoffman, P., Smibert, P., Papalexi, E., and Satija, R. (2018). Integrating single-cell transcriptomic data across different conditions, technologies, and species. *Nat Biotechnol* *36*, 411-420.
- Cahoy, J.D., Emery, B., Kaushal, A., Foo, L.C., Zamanian, J.L., Christopherson, K.S., Xing, Y., Lubischer, J.L., Krieg, P.A., Krupenko, S.A., *et al.* (2008). A transcriptome database for astrocytes, neurons, and oligodendrocytes: a new resource for understanding brain development and function. *J Neurosci* *28*, 264-278.
- Cao, J., Spielmann, M., Qiu, X., Huang, X., Ibrahim, D.M., Hill, A.J., Zhang, F., Mundlos, S., Christiansen, L., Steemers, F.J., *et al.* (2019). The single-cell transcriptional landscape of mammalian organogenesis. *Nature* *566*, 496-502.
- Choi, E., Zhang, X., Xing, C., and Yu, H. (2016). Mitotic Checkpoint Regulators Control Insulin Signaling and Metabolic Homeostasis. *Cell* *166*, 567-581.
- Davidson, I.F., Bauer, B., Goetz, D., Tang, W., Wutz, G., and Peters, J.M. (2019). DNA loop extrusion by human cohesin. *Science* *366*, 1338-1345.

689 De Koninck, M., Lapi, E., Badia-Careaga, C., Cossio, I., Gimenez-Llorente, D., Rodriguez-  
 690 Corsino, M., Andrada, E., Hidalgo, A., Manzanares, M., Real, F.X., *et al.* (2020). Essential Roles  
 691 of Cohesin STAG2 in Mouse Embryonic Development and Adult Tissue Homeostasis. *Cell Rep.*  
 692 32, 108014.

693 De Koninck, M., and Losada, A. (2016). Cohesin Mutations in Cancer. *Cold Spring Harb*  
 694 *Perspect Med* 6.

695 Dixon, J.R., Jung, I., Selvaraj, S., Shen, Y., Antosiewicz-Bourget, J.E., Lee, A.Y., Ye, Z., Kim,  
 696 A., Rajagopal, N., Xie, W., *et al.* (2015). Chromatin architecture reorganization during stem cell  
 697 differentiation. *Nature* 518, 331-336.

698 Dixon, J.R., Selvaraj, S., Yue, F., Kim, A., Li, Y., Shen, Y., Hu, M., Liu, J.S., and Ren, B.  
 699 (2012). Topological domains in mammalian genomes identified by analysis of chromatin  
 700 interactions. *Nature* 485, 376-380.

701 Dobin, A., Davis, C.A., Schlesinger, F., Drenkow, J., Zaleski, C., Jha, S., Batut, P., Chaisson, M.,  
 702 and Gingeras, T.R. (2013). STAR: ultrafast universal RNA-seq aligner. *Bioinformatics* 29, 15-21.

703 Dulken, B.W., Buckley, M.T., Navarro Negredo, P., Saligrama, N., Cayrol, R., Leeman, D.S.,  
 704 George, B.M., Boutet, S.C., Hebestreit, K., Pluvinae, J.V., *et al.* (2019). Single-cell analysis  
 705 reveals T cell infiltration in old neurogenic niches. *Nature* 571, 205-210.

706 Durand, N.C., Shamim, M.S., Machol, I., Rao, S.S., Huntley, M.H., Lander, E.S., and Aiden, E.L.  
 707 (2016). Juicer Provides a One-Click System for Analyzing Loop-Resolution Hi-C Experiments.  
 708 *Cell Syst.* 3, 95-98.

709 Flores-Obando, R.E., Freidin, M.M., and Abrams, C.K. (2018). Rapid and Specific  
 710 Immunomagnetic Isolation of Mouse Primary Oligodendrocytes. *J. Vis. Exp.*

711 Flyamer, I.M., Illingworth, R.S., and Bickmore, W.A. (2020). Coolpup.py: versatile pile-up  
712 analysis of Hi-C data. *Bioinformatics* 36, 2980-2985.

713 Giusti, S.A., Vercelli, C.A., Vogl, A.M., Kolarz, A.W., Pino, N.S., Deussing, J.M., and Refojo,  
714 D. (2014). Behavioral phenotyping of Nestin-Cre mice: implications for genetic mouse models  
715 of psychiatric disorders. *J. Psychiatr. Res.* 55, 87-95.

716 Haarhuis, J.H., Elbatsh, A.M., and Rowland, B.D. (2014). Cohesin and its regulation: on the  
717 logic of X-shaped chromosomes. *Dev. Cell* 31, 7-18.

718 Haarhuis, J.H.I., van der Weide, R.H., Blomen, V.A., Yanez-Cuna, J.O., Amendola, M., van  
719 Ruiten, M.S., Krijger, P.H.L., Teunissen, H., Medema, R.H., van Steensel, B., *et al.* (2017). The  
720 Cohesin Release Factor WAPL Restricts Chromatin Loop Extension. *Cell* 169, 693-707 e614.

721 Hara, K., Zheng, G., Qu, Q., Liu, H., Ouyang, Z., Chen, Z., Tomchick, D.R., and Yu, H. (2014).  
722 Structure of cohesin subcomplex pinpoints direct shugoshin-Wapl antagonism in centromeric  
723 cohesion. *Nat. Struct. Mol. Biol.* 21, 864-870.

724 Heinz, S., Benner, C., Spann, N., Bertolino, E., Lin, Y.C., Laslo, P., Cheng, J.X., Murre, C.,  
725 Singh, H., and Glass, C.K. (2010). Simple combinations of lineage-determining transcription  
726 factors prime cis-regulatory elements required for macrophage and B cell identities. *Mol. Cell* 38,  
727 576-589.

728 Hubler, Z., Allimuthu, D., Bederman, I., Elitt, M.S., Madhavan, M., Allan, K.C., Shick, H.E.,  
729 Garrison, E., M, T.K., Factor, D.C., *et al.* (2018). Accumulation of 8,9-unsaturated sterols drives  
730 oligodendrocyte formation and remyelination. *Nature* 560, 372-376.

731 Kim, Y., Shi, Z., Zhang, H., Finkelstein, I.J., and Yu, H. (2019). Human cohesin compacts DNA  
732 by loop extrusion. *Science* 366, 1345-1349.

733 Kojic, A., Cuadrado, A., De Koninck, M., Gimenez-Llorente, D., Rodriguez-Corsino, M.,  
 734 Gomez-Lopez, G., Le Dily, F., Marti-Renom, M.A., and Losada, A. (2018). Distinct roles of  
 735 cohesin-SA1 and cohesin-SA2 in 3D chromosome organization. *Nat. Struct. Mol. Biol.* 25, 496-  
 736 504.

737 Langmead, B., and Salzberg, S.L. (2012). Fast gapped-read alignment with Bowtie 2. *Nat.*  
 738 *Methods* 9, 357-359.

739 Lazaris, C., Kelly, S., Ntziachristos, P., Aifantis, I., and Tsirigos, A. (2017). HiC-bench:  
 740 comprehensive and reproducible Hi-C data analysis designed for parameter exploration and  
 741 benchmarking. *BMC Genomics* 18, 22.

742 Li, Y., Haarhuis, J.H.I., Seden Cacciatore, A., Oldenkamp, R., van Ruiten, M.S., Willems, L.,  
 743 Teunissen, H., Muir, K.W., de Wit, E., Rowland, B.D., *et al.* (2020). The structural basis for  
 744 cohesin-CTCF-anchored loops. *Nature* 578, 472-476.

745 Liao, Y., Smyth, G.K., and Shi, W. (2014). featureCounts: an efficient general purpose program  
 746 for assigning sequence reads to genomic features. *Bioinformatics* 30, 923-930.

747 Liu, X., Zhang, Y., Chen, Y., Li, M., Zhou, F., Li, K., Cao, H., Ni, M., Liu, Y., Gu, Z., *et al.*  
 748 (2017). In Situ Capture of Chromatin Interactions by Biotinylated dCas9. *Cell* 170, 1028-1043  
 749 e1019.

750 Lopez-Delisle, L., Rabbani, L., Wolff, J., Bhardwaj, V., Backofen, R., Gruning, B., Ramirez, F.,  
 751 and Manke, T. (2020). pyGenomeTracks: reproducible plots for multivariate genomic data sets.  
 752 *Bioinformatics*.

753 Luecken, M.D., and Theis, F.J. (2019). Current best practices in single-cell RNA-seq analysis: a  
 754 tutorial. *Mol Syst Biol* 15, e8746.

755 Mannini, L., Cucco, F., Quarantotti, V., Krantz, I.D., and Musio, A. (2013). Mutation spectrum  
 756 and genotype-phenotype correlation in Cornelia de Lange syndrome. *Hum. Mutat.* *34*, 1589-  
 757 1596.

758 Marques, S., van Bruggen, D., Vanichkina, D.P., Floriddia, E.M., Munguba, H., Varemo, L.,  
 759 Giacomello, S., Falcao, A.M., Meijer, M., Bjorklund, A.K., *et al.* (2018). Transcriptional  
 760 Convergence of Oligodendrocyte Lineage Progenitors during Development. *Dev. Cell* *46*, 504-  
 761 517 e507.

762 Marques, S., Zeisel, A., Codeluppi, S., van Bruggen, D., Mendanha Falcao, A., Xiao, L., Li, H.,  
 763 Haring, M., Hochgerner, H., Romanov, R.A., *et al.* (2016). Oligodendrocyte heterogeneity in the  
 764 mouse juvenile and adult central nervous system. *Science* *352*, 1326-1329.

765 Martincorena, I., and Campbell, P.J. (2015). Somatic mutation in cancer and normal cells.  
 766 *Science* *349*, 1483-1489.

767 Marton, R.M., Miura, Y., Sloan, S.A., Li, Q., Revah, O., Levy, R.J., Huguenard, J.R., and Pasca,  
 768 S.P. (2019). Differentiation and maturation of oligodendrocytes in human three-dimensional  
 769 neural cultures. *Nat. Neurosci.* *22*, 484-491.

770 Mathys, H., Davila-Velderrain, J., Peng, Z., Gao, F., Mohammadi, S., Young, J.Z., Menon, M.,  
 771 He, L., Abdurrob, F., Jiang, X., *et al.* (2019). Single-cell transcriptomic analysis of Alzheimer's  
 772 disease. *Nature* *570*, 332-337.

773 McDonald, J.G., Smith, D.D., Stiles, A.R., and Russell, D.W. (2012). A comprehensive method  
 774 for extraction and quantitative analysis of sterols and secosteroids from human plasma. *J. Lipid*  
 775 *Res.* *53*, 1399-1409.

776 Mitew, S., Hay, C.M., Peckham, H., Xiao, J., Koenning, M., and Emery, B. (2014). Mechanisms  
777 regulating the development of oligodendrocytes and central nervous system myelin.  
778 *Neuroscience* 276, 29-47.

779 Moore, M.J., and Proudfoot, N.J. (2009). Pre-mRNA processing reaches back to transcription  
780 and ahead to translation. *Cell* 136, 688-700.

781 Pan, H., Jin, M., Ghadiyaram, A., Kaur, P., Miller, H.E., Ta, H.M., Liu, M., Fan, Y., Mahn, C.,  
782 Gorthi, A., *et al.* (2020). Cohesin SA1 and SA2 are RNA binding proteins that localize to RNA  
783 containing regions on DNA. *Nucleic Acids Res.* 48, 5639-5655.

784 Piche, J., Van Vliet, P.P., Puceat, M., and Andelfinger, G. (2019). The expanding phenotypes of  
785 cohesinopathies: one ring to rule them all! *Cell Cycle* 18, 2828-2848.

786 Porter, H., Li, Y., Varsally, W., Neguembor, M.V., Beltran, M., Pezic, D., Martin, L., Cornejo,  
787 M.T., Bhamra, A., Surinova, S., *et al.* (2021). STAG proteins promote cohesin ring loading at R-  
788 loops. *bioRxiv*, 2021.2002.2020.432055.

789 Rao, S.S.P., Huang, S.C., Glenn St Hilaire, B., Engreitz, J.M., Perez, E.M., Kieffer-Kwon, K.R.,  
790 Sanborn, A.L., Johnstone, S.E., Bascom, G.D., Bochkov, I.D., *et al.* (2017). Cohesin Loss  
791 Eliminates All Loop Domains. *Cell* 171, 305-320 e324.

792 Remeseiro, S., Cuadrado, A., Carretero, M., Martinez, P., Drosopoulos, W.C., Canamero, M.,  
793 Schildkraut, C.L., Blasco, M.A., and Losada, A. (2012). Cohesin-SA1 deficiency drives  
794 aneuploidy and tumourigenesis in mice due to impaired replication of telomeres. *EMBO J.* 31,  
795 2076-2089.

796 Remeseiro, S., Cuadrado, A., Kawauchi, S., Calof, A.L., Lander, A.D., and Losada, A. (2013a).  
797 Reduction of Nipbl impairs cohesin loading locally and affects transcription but not cohesion-

798 dependent functions in a mouse model of Cornelia de Lange Syndrome. *Biochim. Biophys. Acta*  
799 *1832*, 2097-2102.

800 Remeseiro, S., Cuadrado, A., and Losada, A. (2013b). Cohesin in development and disease.  
801 *Development* *140*, 3715-3718.

802 Robinson, M.D., McCarthy, D.J., and Smyth, G.K. (2010). edgeR: a Bioconductor package for  
803 differential expression analysis of digital gene expression data. *Bioinformatics* *26*, 139-140.

804 Ross-Innes, C.S., Stark, R., Teschendorff, A.E., Holmes, K.A., Ali, H.R., Dunning, M.J., Brown,  
805 G.D., Gojis, O., Ellis, I.O., Green, A.R., *et al.* (2012). Differential oestrogen receptor binding is  
806 associated with clinical outcome in breast cancer. *Nature* *481*, 389-393.

807 Saher, G., Brugger, B., Lappe-Siefke, C., Mobius, W., Tozawa, R., Wehr, M.C., Wieland, F.,  
808 Ishibashi, S., and Nave, K.A. (2005). High cholesterol level is essential for myelin membrane  
809 growth. *Nat. Neurosci.* *8*, 468-475.

810 Saunders, A., Macosko, E.Z., Wysoker, A., Goldman, M., Krienen, F.M., de Rivera, H., Bien, E.,  
811 Baum, M., Bortolin, L., Wang, S., *et al.* (2018). Molecular Diversity and Specializations among  
812 the Cells of the Adult Mouse Brain. *Cell* *174*, 1015-1030 e1016.

813 Schwarzer, W., Abdennur, N., Goloborodko, A., Pekowska, A., Fudenberg, G., Loe-Mie, Y.,  
814 Fonseca, N.A., Huber, W., Haering, C.H., Mirny, L., *et al.* (2017). Two independent modes of  
815 chromatin organization revealed by cohesin removal. *Nature* *551*, 51-56.

816 Servant, N., Varoquaux, N., Lajoie, B.R., Viara, E., Chen, C.J., Vert, J.P., Heard, E., Dekker, J.,  
817 and Barillot, E. (2015). HiC-Pro: an optimized and flexible pipeline for Hi-C data processing.  
818 *Genome Biol* *16*, 259.

819 Shi, Z., Gao, H., Bai, X.C., and Yu, H. (2020). Cryo-EM structure of the human cohesin-NIPBL-  
820 DNA complex. *Science* *368*, 1454-1459.

821 Soardi, F.C., Machado-Silva, A., Linhares, N.D., Zheng, G., Qu, Q., Pena, H.B., Martins,  
822 T.M.M., Vieira, H.G.S., Pereira, N.B., Melo-Minardi, R.C., *et al.* (2017). Familial STAG2  
823 germline mutation defines a new human cohesinopathy. *NPJ Genom. Med.* 2, 7.

824 Stuart, T., Butler, A., Hoffman, P., Hafemeister, C., Papalexi, E., Mauck, W.M., 3rd, Hao, Y.,  
825 Stoeckius, M., Smibert, P., and Satija, R. (2019). Comprehensive Integration of Single-Cell Data.  
826 *Cell* 177, 1888-1902 e1821.

827 Thakurela, S., Garding, A., Jung, R.B., Muller, C., Goebbels, S., White, R., Werner, H.B., and  
828 Tiwari, V.K. (2016). The transcriptome of mouse central nervous system myelin. *Sci. Rep.* 6,  
829 25828.

830 Tronche, F., Kellendonk, C., Kretz, O., Gass, P., Anlag, K., Orban, P.C., Bock, R., Klein, R., and  
831 Schutz, G. (1999). Disruption of the glucocorticoid receptor gene in the nervous system results in  
832 reduced anxiety. *Nat. Genet.* 23, 99-103.

833 Tsirigos, A., Haiminen, N., Bilal, E., and Utro, F. (2012). GenomicTools: a computational  
834 platform for developing high-throughput analytics in genomics. *Bioinformatics* 28, 282-283.

835 Uhlmann, F. (2016). SMC complexes: from DNA to chromosomes. *Nat. Rev. Mol. Cell Biol.* 17,  
836 399-412.

837 van der Weide, R.H., van den Brand, T., Haarhuis, J.H.I., Teunissen, H., Rowland, B.D., and de  
838 Wit, E. (2021). Hi-C analyses with GENOVA: a case study with cohesin variants. *NAR Genom*  
839 *Bioinform* 3, lqab040.

840 van Tilborg, E., van Kammen, C.M., de Theije, C.G.M., van Meer, M.P.A., Dijkhuizen, R.M.,  
841 and Nijboer, C.H. (2017). A quantitative method for microstructural analysis of myelinated  
842 axons in the injured rodent brain. *Sci. Rep.* 7, 16492.

843 Ventura, A., Kirsch, D.G., McLaughlin, M.E., Tuveson, D.A., Grimm, J., Lintault, L., Newman,  
844 J., Reczek, E.E., Weissleder, R., and Jacks, T. (2007). Restoration of p53 function leads to  
845 tumour regression in vivo. *Nature* *445*, 661-665.

846 Vian, L., Pekowska, A., Rao, S.S.P., Kieffer-Kwon, K.R., Jung, S., Baranello, L., Huang, S.C.,  
847 El Khattabi, L., Dose, M., Pruett, N., *et al.* (2018). The Energetics and Physiological Impact of  
848 Cohesin Extrusion. *Cell* *175*, 292-294.

849 Vuilleumier, N., Kovari, E., Michon, A., Hof, P.R., Mentenopoulos, G., Giannakopoulos, P., and  
850 Bouras, C. (2002). Neuropathological analysis of an adult case of the Cornelia de Lange  
851 syndrome. *Acta Neuropathol.* *104*, 327-332.

852 Williamson, J.M., and Lyons, D.A. (2018). Myelin Dynamics Throughout Life: An Ever-  
853 Changing Landscape? *Front. Cell Neurosci.* *12*, 424.

854 Wingett, S. (2011). FastQ Screen: quality control tool to screen a library of sequences in FastQ  
855 format against a set of sequence databases. .

856 Wolf, N.I., French-Constant, C., and van der Knaap, M.S. (2021). Hypomyelinating  
857 leukodystrophies - unravelling myelin biology. *Nat. Rev. Neurol.* *17*, 88-103.

858 Wutz, G., Ladurner, R., St Hilaire, B.G., Stocsits, R.R., Nagasaka, K., Pignard, B., Sanborn, A.,  
859 Tang, W., Varnai, C., Ivanov, M.P., *et al.* (2020). ESCO1 and CTCF enable formation of long  
860 chromatin loops by protecting cohesin(STAG1) from WAPL. *eLife* *9*.

861 Wutz, G., Varnai, C., Nagasaka, K., Cisneros, D.A., Stocsits, R.R., Tang, W., Schoenfelder, S.,  
862 Jessberger, G., Muhar, M., Hossain, M.J., *et al.* (2017). Topologically associating domains and  
863 chromatin loops depend on cohesin and are regulated by CTCF, WAPL, and PDS5 proteins.  
864 *EMBO J.* *36*, 3573-3599.

865 Yatskevich, S., Rhodes, J., and Nasmyth, K. (2019). Organization of Chromosomal DNA by  
866 SMC Complexes. *Annu. Rev. Genet.* 53, 445-482.

867 Zeisel, A., Hochgerner, H., Lonnerberg, P., Johnsson, A., Memic, F., van der Zwan, J., Haring,  
868 M., Braun, E., Borm, L.E., La Manno, G., *et al.* (2018). Molecular Architecture of the Mouse  
869 Nervous System. *Cell* 174, 999-1014 e1022.

870 Zhang, Y., Liu, T., Meyer, C.A., Eeckhoute, J., Johnson, D.S., Bernstein, B.E., Nusbaum, C.,  
871 Myers, R.M., Brown, M., Li, W., *et al.* (2008). Model-based analysis of ChIP-Seq (MACS).  
872 *Genome Biol.* 9, R137.

873 Zheng, G., and Yu, H. (2015). Regulation of sister chromatid cohesion during the mitotic cell  
874 cycle. *Sci. China Life Sci.* 58, 1089-1098.

875 Zywitza, V., Misios, A., Bunatyan, L., Willnow, T.E., and Rajewsky, N. (2018). Single-Cell  
876 Transcriptomics Characterizes Cell Types in the Subventricular Zone and Uncovers Molecular  
877 Defects Impairing Adult Neurogenesis. *Cell Rep.* 25, 2457-2469 e2458.

878

879

880

## Figure legends

**Figure 1.** *Stag2* ablation in the mouse nervous system causes growth retardation and neurological defects. (A) Scheme for creating the “floxed” *Stag2* allele by gene targeting. The genomic structure of the wild-type (WT) *Stag2* locus, the targeting vector, the knock-in allele, the disrupted allele after Cre-mediated recombination, and the positions of the genotyping primers are shown. The amino acid sequence of the knockout allele in the targeted region is shown and aligned with that of the WT allele. (B) PCR analysis of the genomic DNA extracted from the tails of indicated mice with the primers in (A). (C) PCR analysis of genomic DNA extracted from brains (BR) or livers (LV) of indicated mice. (D) Immunoblots of brain lysates of *Stag2<sup>f/y</sup>* and *Stag2<sup>f/y</sup>;Nes<sup>Cre</sup>* mice with antibodies recognizing cohesin subunits and TUBULIN (as the loading control). (E) Representative images of *Stag2<sup>f/y</sup>* and *Stag2<sup>f/y</sup>;Nes<sup>Cre</sup>* mice. Scale bar = 2 cm. (F) Body weight of *Stag2<sup>f/y</sup>* and *Stag2<sup>f/y</sup>;Nes<sup>Cre</sup>* mice at different age. Mean  $\pm$  SD of at least three mice of the same age. (G) Survival curves of *Stag2<sup>f/y</sup>* (n = 12) and *Stag2<sup>f/y</sup>;Nes<sup>Cre</sup>* (n = 21) mice. (H,I) Food (H) and water (I) consumption of 7- to 8-week-old *Stag2<sup>f/y</sup>* (n = 6) and *Stag2<sup>f/y</sup>;Nes<sup>Cre</sup>* (n = 4) mice. Mean  $\pm$  SD; ns, not significant. (J) Plasma IGF-1 levels of two-month-old *Stag2<sup>f/y</sup>* (n = 5) and *Stag2<sup>f/y</sup>;Nes<sup>Cre</sup>* (n = 6) mice. Mean  $\pm$  SD; \*\*\*\*p < 0.0001. (K) Representative images of limb-clasping responses of *Stag2<sup>f/y</sup>* and *Stag2<sup>f/y</sup>;Nes<sup>Cre</sup>* mice. The uncropped images of blots in (B–D) are included in Figure 1 source data 1.

**Figure 2.** *Stag2* ablation in mouse brains downregulates the expression of myelin genes. (A) Volcano plot of bulk RNA sequencing results of *Stag2<sup>f/y</sup>* and *Stag2<sup>f/y</sup>;Nes<sup>Cre</sup>* brain extracts. Top differentially expressed genes (DEGs) are colored blue and labeled. n = 4 pairs of P21 *Stag2<sup>f/y</sup>* and *Stag2<sup>f/y</sup>;Nes<sup>Cre</sup>* brain hemispheres were used for the comparison. (B) RT-qPCR analysis of

the top downregulated genes in the brain extracts.  $n = 4$  pairs of *Stag2<sup>f/y</sup>* and *Stag2<sup>f/y</sup>;Nes<sup>Cre</sup>* littermates were used. Mean  $\pm$  SD. (C) Heatmap of the expression of myelin-enriched genes that were down-regulated by more than two folds in *Stag2<sup>f/y</sup>;Nes<sup>Cre</sup>* brains. *L1* and *R1*, left and right brain hemispheres of the *Stag2<sup>f/y</sup>#1* mouse. *L2* and *R2*, left and right brain hemispheres of the *Stag2<sup>f/y</sup>#2* mouse. *L1'* and *R1'*, left and right brain hemispheres of the *Stag2<sup>f/y</sup>;Nes<sup>Cre</sup> #1* mouse. *L2'* and *R2'*, left and right brain hemispheres of the *Stag2<sup>f/y</sup>;Nes<sup>Cre</sup>#2* mouse. The biological pathways of these genes are labeled on the right. (D) The top five canonical pathways identified by ingenuity pathway analysis (IPA) of the DEGs. The complete gene list is used as the background.

**Figure 3.** *Stag2* ablation in the nervous system compromises myelination during early postnatal development. (A) Luxol fast blue staining of the sagittal sections of *Stag2<sup>f/y</sup>* and *Stag2<sup>f/y</sup>;Nes<sup>Cre</sup>* brains.  $n = 3$  animals per genotype. Scale bar = 1 mm. (B) Immunohistochemistry staining with the anti-MBP antibody in the cerebral cortex (left panel). Antibody-stained areas and DAPI staining regions are marked with red and yellow dashed lines, respectively. Scale bar = 200  $\mu$ m. Quantification of the percentage of the myelinated cortex is shown in the right panel.  $n = 4$  pairs of *Stag2<sup>f/y</sup>* and *Stag2<sup>f/y</sup>;Nes<sup>Cre</sup>* littermates were used (P18 or P21) for the comparison.  $**p < 0.01$ ; Mean  $\pm$  SD. (C) Immunohistochemistry staining with the anti-PLP1 antibody in the cerebellum (left panel). Antibody-stained areas and DAPI staining regions are marked with red and yellow dashed lines, respectively. Scale bar = 200  $\mu$ m. Quantification of the percentage of the myelinated cerebellum granular layer is shown in the right panel.  $n = 3$  pairs of *Stag2<sup>f/y</sup>* and *Stag2<sup>f/y</sup>;Nes<sup>Cre</sup>* littermates were used (P20 or P25) for the comparison.  $*p < 0.05$ ; Mean  $\pm$  SD. (D) Higher magnification images (left panel) of the immunohistochemistry staining with the anti-

MBP antibody in (B). Images processed through axial thinning are shown in the right panel. Scale bar = 50  $\mu$ m. (E,F) Total fiber length (E) and fiber coherency (F) measured using the processed images in (D). n = 4 pairs of *Stag2<sup>f/y</sup>* and *Stag2<sup>f/y</sup>;Nes<sup>Cre</sup>* littermates were used (P18 or P21). \*p < 0.05, \*\*p < 0.01; Mean  $\pm$  SD. (G) Transmission electron microscopy images of the optic nerves (left panel). Scale bar = 2  $\mu$ m. Quantification of myelinated axon distributions is shown in the right panel. n = 4 pairs of P18 *Stag2<sup>f/y</sup>* and *Stag2<sup>f/y</sup>;Nes<sup>Cre</sup>* littermates were used. n  $\geq$  10 fields of each mouse were taken, and the average distribution of myelinated axons were calculated for each mouse and plotted. \*\*p < 0.01; Mean  $\pm$  SD.

**Figure 4.** Deletion of *Stag2* in mouse brains causes differentiation delay and transcriptional changes in oligodendrocytes. (A) *t*-SNE plot of cell clusters in *Stag2<sup>f/y</sup>* and *Stag2<sup>f/y</sup>;Nes<sup>Cre</sup>* forebrains analyzed by single-cell RNA-seq (scRNA-seq). n = 2 mice of each genotype were used in the scRNA-seq analysis. aNSCs/NPCs, active neural stem cells or neural progenitor cells; Astrocytes/qNSCs, astrocytes or quiescent neural stem cells; OPCcycs, cycling oligodendrocyte (OL) progenitor cells; OPCs, OL progenitor cells; NFOLs, newly formed OLs; mFOLs, myelin-forming OLs; MOLs, matured OLs; VLMCs, vascular and leptomeningeal cells; vSMCs, vascular smooth muscle cells. (B) *t*-SNE clustering as in (A) but colored by genotype. (C) Left panel: cell type composition and percentage as colored in (A). Right panel: percentage of cell clusters of the oligodendrocyte lineage. (D) FeaturePlot of a representative gene (*Mal*) specifically suppressed in MOLs of *Stag2<sup>f/y</sup>;Nes<sup>Cre</sup>* forebrains. A maximum cutoff of 3 was used. (E) Experimental scheme of the magnetic-activated cell sorting (MACS) of primary OLs. (F) Volcano plot of bulk RNA-seq results of *Stag2<sup>f/y</sup>* and *Stag2<sup>f/y</sup>;Nes<sup>Cre</sup>* primary OLs. (G) The top five canonical pathways identified by IPA of the DEGs with more than 2-fold change in (F).

The complete gene list is used as the background. (H) Commons DEGs shared between bulk RNA-seq analyses of the whole brains (WB) and primary OLs.

**Figure 5.** Enrichment of STAG2 and histone modifications at gene promoters. (A) Heatmap of H3K27ac ChIP-seq signal enrichment in the promoter regions of genes in the indicated categories. (B) Density profile of H3K27ac ChIP-seq signal enrichment in the promoter regions of genes in the indicated categories as in (A). (C) Density profile of STAG2 ChIP-seq signal enrichment in the promoter regions of genes in the indicated categories as in (A). (D) Binding of STAG2 at the genomic loci of down-regulated genes that encode cholesterol biosynthetic enzymes as revealed by ChIP-seq.

**Figure 6. Loss of *Stag2* does not alter compartments and TADs in oligodendrocytes.** (A) Representative snapshots of balanced Hi-C contact matrices of chromosome 2. Tracks of eigenvector-1 fixed with housekeeping genes are shown below, with A and B compartments shown in red and blue, respectively. (B) Hexbin plot of eigenvector-1 for genomic bins (100 kb) in *Stag2<sup>f/y</sup>* and *Stag2<sup>f/y</sup>;Nes<sup>Cre</sup>* oligodendrocytes (OLs). (C) Chromatin bins were classified into four categories based on the eigenvector sign and whether it has switched with a delta bigger than 1.5. AB, changing from compartment A in *Stag2<sup>f/y</sup>* to compartment B in *Stag2<sup>f/y</sup>;Nes<sup>Cre</sup>*; BA, from B in *Stag2<sup>f/y</sup>* to A in *Stag2<sup>f/y</sup>;Nes<sup>Cre</sup>*; AA, A in both *Stag2<sup>f/y</sup>* and *Stag2<sup>f/y</sup>;Nes<sup>Cre</sup>*; BB, B in both *Stag2<sup>f/y</sup>* and *Stag2<sup>f/y</sup>;Nes<sup>Cre</sup>*. (D) Boxplot of averaged gene expression change of DEGs (RNA logFC cutoff of  $\pm 0.58$ ) inside each genomic bin. Bins counted: AA, 1646; AB, 56; BA, 69; BB, 910. Red dots represent the mean value. An unpaired Wilcoxon test was used for the statistical analysis. \*p < 0.05; \*\*p < 0.01; \*\*\*p < 0.001; ns, not significant. (E,F) Principal

component (E) and similarity (F) analysis performed using the insulation score at 10 kb resolution. (G) Aggregate TAD analysis on the 10 kb merged Hi-C matrices using TADs called from the merged samples of *Stag2*<sup>f/y</sup> at 10 kb resolution.

**Figure 7.** *Stag2* deletion impairs the formation of total and promoter-anchored loops in oligodendrocytes. (A) Loop counts (left panel) and length (right panel) in the indicated categories of *Stag2*<sup>f/y</sup> and *Stag2*<sup>f/y</sup>;*Nes*<sup>Cre</sup> oligodendrocytes (OLs). (B) Loop counts plotted against loop length (from 0 to 5 Mb) of *Stag2*<sup>f/y</sup> and *Stag2*<sup>f/y</sup>;*Nes*<sup>Cre</sup> OLs. (C) Normalized contact counts for loops across different genomic distances in *Stag2*<sup>f/y</sup> and *Stag2*<sup>f/y</sup>;*Nes*<sup>Cre</sup> OLs. (D) Representative snapshots of contact maps at the *Mal* gene locus. .hic files generated by HiC-Pro were converted to .cool format for plotting at 5kb resolution. Tracks and narrow peaks from STAG2 and H3K27ac ChIP-seq as well as the loops are plotted below. Transcription direction is indicated by the black arrow. (E) Pile-up analysis of loop “dots”-centered local maps for the promoter-anchored loops of genes in the indicated categories. The maps are balanced, normalized by distance, and plotted at 5 kb resolution. The numbers indicate the enrichment of the central pixel over the upper left and bottom right corners. (F) Pile-up analysis of the local contact maps centered around the transcription start site (TSS) of genes in the indicated categories. Transcription directions are indicated below. 1,000 stable genes are chosen randomly and used for the analysis. The maps are balanced, normalized by distance, and plotted at 5kb resolution. Diagonal pixels are omitted.

**Figure 8.** Proposed roles of STAG2-cohesin-mediated loop extrusion during transcription in oligodendrocytes. (A) STAG2-cohesin-mediated chromosome looping connects the enhancer

996 and the promoter, thus facilitating interactions among oligodendrocyte-specific transcription  
997 factors, the mediator complex, and the general transcription machinery including RNA  
998 polymerase II. (B) STAG2-cohesin travels along the gene body via transcription-coupled loop  
999 extrusion to facilitate pre-mRNA processing. (C) STAG2-cohesin mediates the formation of  
1000 gene loops that bring the terminator close to the promoter and facilitate Pol II recycling for  
1001 multiple rounds of transcription.

1002

## Figure Supplements

**Figure 1—Figure Supplement 1.** Generation of *Stag2* knockout mice using the CRISPR/Cas9 method. (A) Scheme for disrupting *Stag2* in the mouse genome using CRISPR/Cas9 with guide RNAs flanking exon 8. Sequencing analysis of the genomic DNA extracted from two *Stag2*-disrupted founder mice is shown below. (B) Hematoxylin and eosin (H&E) staining of sagittal sections of F2 embryos derived from F1 in (A) at E11.5.

**Figure 1—Figure Supplement 2.** Generation of *Stag2* conditional knockout mice by gene targeting. (A) Experimental scheme of tamoxifen injection into adult *Stag2<sup>f/y</sup>;Rosa26<sup>CreErt2</sup>* and *Stag2<sup>+/y</sup>;Rosa26<sup>CreErt2</sup>* mice. (B) Western blotting of cell extracts from *Stag2<sup>f/y</sup>;Rosa26<sup>CreErt2</sup>* mouse embryonic fibroblasts (MEF) treated with or without 4-hydroxytamoxifen (4OHT). E12.5 MEFs were prepared from *Stag2<sup>f/y</sup>;Rosa26<sup>CreErt2</sup>* mouse embryos and subjected to 4OHT treatment. (C) PCR analysis of the genomic DNA extracted from the blood of indicated mice with the primers in Figure 1A. Only the floxed mice carrying *Rosa26<sup>CreErt2</sup>* (1,2,3,7,8) had their exon 8 excised in the condition of tamoxifen injection. (D) Survival curves of *Stag2<sup>f/y</sup>;Rosa26<sup>CreErt2</sup>* (n=26) and *Stag2<sup>+/y</sup>;Rosa26<sup>CreErt2</sup>* (n=19) mice after tamoxifen injection. (E) Body weight of mice in (D). (F) Body weight of *Stag2<sup>f/y</sup>;Rosa26<sup>CreErt2</sup>* (n=20) and *Stag2<sup>+/y</sup>;Rosa26<sup>CreErt2</sup>* (n=18) mice at 6 months post tamoxifen injection. \*\*\*\*-p<0.0001. Uncropped images of gels and blots in this figure are included in Figure 1—Figure Supplement 2 source data 1.

**Figure 2—Figure Supplement 1.** STAG2 deficiency in mouse brains attenuates cholesterol biosynthesis. (A) H&E staining of the coronal sections of *Stag2<sup>f/y</sup>* and *Stag2<sup>f/y</sup>;Nes<sup>Cre</sup>* mouse

brains. Scale bar, 1 mm. **(B,C)** Immunohistochemistry staining of signature proteins of astrocytes **(B)** and neurons **(C)** on brain coronal sections of *Stag2<sup>f/y</sup>* and *Stag2<sup>f/y</sup>;Nes<sup>Cre</sup>* mice. Scale bar = 100  $\mu$ m. **(D)** Density of GFAP<sup>+</sup> astrocytes in the cornu ammonis (CA) area (outlined with white dash lines in **B**) of the hippocampus. **(E)** Density of MAP2<sup>+</sup> neurons in the dentate gyrus hilus (outlined with white dash lines in **C**). **(F)** Mass spectrometry analysis of cholesterol precursors in *Stag2<sup>f/y</sup>* and *Stag2<sup>f/y</sup>;Nes<sup>Cre</sup>* brains. n = 3 mice per genotype. \*p < 0.05, \*\*p < 0.01, \*\*\*p < 0.001; Mean  $\pm$  SD.

**Figure 2—Figure Supplement 2.** Over-representation analysis (ORA) of the RNA-seq results of the mouse brain samples. **(A,B)** The enriched biological pathways identified by gene ontology of ClusterProfiler from the down-regulated genes **(A)** or up-regulated genes **(B)** with >2-fold change between *Stag2<sup>f/y</sup>* and *Stag2<sup>f/y</sup>;Nes<sup>Cre</sup>* mice from the whole-brain RNA-seq dataset. Pathways of gliogenesis and myelination are highlighted in red. Pathways of membrane lipid biosynthesis are colored in blue. The top 20 pathways with the highest gene ratio are presented. **(C,D)** Similarity tree plot of the top 30 enriched biological pathway as identified in **A** for the down-regulated genes **(C)** or as in **B** for the up-regulated genes **(D)**. Pathways of myelination and gliogenesis are highlighted in red. Pathways of fatty acid biosynthesis and membrane lipid biosynthesis related to myelin sheath formation are colored in pink and blue, respectively.

**Figure 3—Figure Supplement 1.** Brain-specific *Stag2* deletion impairs CNS myelination. **(A)** Luxol fast blue staining of the coronal brain sections of mice with the indicated genotypes. n = 3 mice each for *Stag2<sup>f/y</sup>* and *Stag2<sup>f/y</sup>;Nes<sup>Cre</sup>* genotypes. n = 2 mice each for WT and *Nes<sup>Cre</sup>/+* groups. animals per genotype. Scale bar = 1 mm. **(B)** In situ hybridization of <sup>35</sup>S-labeled RNA

probes of the coronal (left) and sagittal (right) sections of WT mouse brains. Bright field images (purple) were overlaid with autoradiography images (red). Scale bar = 1 mm.

**Figure 4—Figure Supplement 1.** *Stag2* is ablated during early neural lineage differentiation of *Stag2* knockout mice. (A) Violin plot of the expression levels of feature genes of the indicated brain cell types. (B–D) Dotplot showing the expression levels of cohesin subunit genes in the oligodendrocyte lineages (OLs; B), astrocytes (C) and neurons (D) and in the progenitor cells. *Stag2* expression is greatly diminished in the neuronal stem cells (NSCs) or neuronal progenitor cells (NPCs).

**Figure 4—Figure Supplement 2.** *Stag2* deletion causes differentiation delay in the oligodendrocyte lineage. (A) Trajectory inference analysis of oligodendrocyte (OL) lineage cells extracted from the single-cell RNA-seq dataset using Monocle3. Cells are colored from purple to yellow by pseudotime variables. (B) OL differentiation trajectory in the *t-SNE* plot. The OL lineage is colored from navy blue to yellow by pseudotime variables. Cells of other lineages are colored grey. (C) Distribution of the assigned OL cell types along the trajectory. (D) Heatmap of gene expression dynamics over pseudotime along the OL differentiation trajectory. Each row represents one of the top 100 most variable genes along pseudotime. Each column represents a single cell. (E) Re-clustered OL subgroups in the trajectory inference analysis. (F) Cell density across pseudotime for the OL differentiation trajectory. Dominant clusters for each pseudotime bin are color labeled as in (E).

**Figure 4—Figure Supplement 3.** STAG2 regulates the transcription of oligodendrocyte genes. (A) FeaturePlot of the expression levels of representative down-regulated genes in the

*Stag2<sup>f/y</sup>;Nes<sup>Cre</sup>* whole brains. Maximum cutoff of 3 was used. (B) Violin plot of the expression of cohesin subunit genes in the indicated brain cell types from the scRNA-seq transcriptome analysis. (C) FeaturePlot of the expression of *Stag1* and *Stag2* in *Stag2<sup>f/y</sup>* and *Stag2<sup>f/y</sup>;Nes<sup>Cre</sup>* forebrains. Maximum cutoff of 3 was used.

**Figure 4—Figure Supplement 4. STAG2 regulates transcription in primary oligodendrocytes.**

(A) The expression levels of signature genes of indicated brain cell types in the isolated primary oligodendrocytes (OLs) in this study. The expression levels of the same set of signature genes in the individually isolated cell types from previous studies are shown below. NFOL and mFOL signature genes are highly enriched in the isolated primary OLs in this study. (B) Boxplot of the expression levels for genes in the indicated categories. Red dots represent the mean values. \*\*\* $p < 0.001$ . Differentially expressed genes with more than 1.5-fold change are assigned as “down” or “up”. Active genes with logFC between  $\pm 0.38$  are assigned “stable”. (C) Violin plot of the expression changes for the active genes with different expression levels. Red dots represent the mean value. \*\*\* $p < 0.001$ . DEGs of the indicated categories are highlighted in red and blue. (D) Scatter plot of the gene expression level against transcriptional changes. (E) IPA analysis of the down-regulated gene sets. The top 5 canonical pathways identified from IPA analysis of the down-regulated genes in *Stag2*-deleted OLs. Down-regulated genes with  $> 2$ -fold change were included in the analysis.

**Figure 4—Figure Supplement 5. Over-representation analysis (ORA) of the down-regulated genes in *Stag2*-deleted oligodendrocytes.** (A) The enriched biological pathways identified from the down-regulated genes with  $> 2$ -fold change in the *Stag2*-deleted primary oligodendrocytes.

The top 20 pathways with the highest gene ratio are presented. **(B)** Treeplot of the top 30 enriched biological pathways identified as in **(A)**. Pathways are grouped and colored by similarity. **(C)** Overlapped genes among the enriched biological pathways. Bar graph shows the number of overlapped genes among biological pathways. **(D)** Heatmap of the top enriched biological pathways and the expression change of related genes. **(E)** IPA analysis of the down-regulated gene sets. The top 5 canonical pathways identified from IPA analysis of the down-regulated genes in *Stag2*-depleted OLs. Down-regulated genes with > 2-fold change were included in the analysis.

**Figure 4—Figure Supplement 6.** Over-representation analysis (ORA) of the up-regulated genes in *Stag2*-deleted oligodendrocytes. **(A)** The enriched biological pathways identified from the up-regulated genes with >2-fold change in the *Stag2*-depleted primary oligodendrocytes. The top 20 pathways with the highest gene ratio are presented. **(B)** Overlapped genes among the enriched biological pathways. Bar graph shows the number of overlapped genes among biological pathways. **(C)** Heatmap of the top enriched biological pathways and the expression change of related genes.

**Figure 5—Figure Supplement 1.** STAG2 occupies the promoters of myelination genes. Tracks of STAG2 binding at the genomic loci of the down-regulated myelination genes. Red arrows indicate the transcription direction.

**Figure 6—Figure Supplement 1.** *Stag2*-deleted OLs do not present significant changes in compartments and TADs. **(A)** HiCRep analysis for reproducibility of the Hi-C replicates. The

stratum-adjusted correlation coefficient (SCC) is calculated for each pair of duplicates for all chromosomes at 25kb resolution. **(B)** Compartment compositions of the indicated samples. **(C)** Boxplot of the average gene expression change for all the differentially expressed genes (FDR < 0.05) inside each genomic bin. Bins counted: AA, 5806; AB, 155; BA, 251; BB, 2659. The unpaired Wilcoxon-test was used for the statistical analysis. \*p < 0.05; \*\*p < 0.01; \*\*\*p < 0.001; ns, not significant. **(D)** Aggregate TAD analysis on the replicates of 10-kb Hi-C matrices using TADs called from the merged samples of *Stag2<sup>f/y</sup>* at 10- or 25-kb resolution. **(E)** Hi-C sample statistics of total read pairs, valid pairs, and cis-pairs using HiC-Pro.

**Figure 7—Figure Supplement 1. *Stag2* deletion reduces chromatin loops in oligodendrocytes.** **(A)** Loop numbers of the indicated categories. **(B)** Aggregate peak analysis on the replicates of 10-kb Hi-C matrices using loops called from the merged samples of *Stag2<sup>f/y</sup>* or *Stag2<sup>f/y</sup>;Nes<sup>Cre</sup>* mice. **(C,D)** Aggregate peak analysis performed on the replicates of 10-kb Hi-C matrices using the group-specific loops. *Stag2<sup>f/y</sup>*-specific loops are used in **(C)** and *Stag2<sup>f/y</sup>;Nes<sup>Cre</sup>*-specific loops are used in **(D)**. The log<sub>2</sub> fold change over *Stag2<sup>f/y</sup> #1* is plotted on the top panels. **(E)** Pile-up analysis of loop “dots”-centered local contact maps for loops specific to *Stag2<sup>f/y</sup>* or *Stag2<sup>f/y</sup>;Nes<sup>Cre</sup>* oligodendrocytes (OLs). **(F)** Hexbin plot of contact counts of common loops in *Stag2<sup>f/y</sup>* and *Stag2<sup>f/y</sup>;Nes<sup>Cre</sup>* OLs. **(G)** Scatter plot of contact counts of common loops in *Stag2<sup>f/y</sup>* and *Stag2<sup>f/y</sup>;Nes<sup>Cre</sup>* OLs. Loops with significantly changed strength in *Stag2<sup>f/y</sup>;Nes<sup>Cre</sup>* OLs are highlighted in red (increased) and blue (decreased). Log<sub>2</sub>FC threshold of 1 was used. **(H)** Normalized contact counts for loops in the indicated categories across different genomic distances.

**Figure 7—Figure Supplement 2.** STAG2 controls local chromatin looping at differentially expressed genes. (A–C) Snapshots of the contact maps at the indicated differentially expressed genes. Tracks and peaks from STAG2 and H3K27ac ChIP-seq as well as loops are shown below. Transcription directions are indicated by arrows. (D) Representative snapshots of contact maps of the replicate samples at *Mal* and *Nkx6-2* genomic loci. .hic files generated by HiC-Pro were converted into .cool format. Graphs were plotted with pyGenomeTracks at 5-kb resolution. Transcription orientations are indicated with the black arrows.

**Figure 7—Figure Supplement 3.** STAG2 regulates the formation of promoter-anchored loops in oligodendrocytes. (A) Loop counts (left panel) and fractions (right panel) of loops anchored at promoter or non-promoter regions in the indicated categories. (B) Loop score of the loops in Figure 7E. Loop score from *Stag2<sup>f/y</sup>* oligodendrocytes (OLs) was used for common loops on the left, and loop score from *Stag2<sup>f/y</sup>;Nes<sup>Cre</sup>* OLs was used for common loops on the right. The unpaired Wilcoxon test was used for the statistical analysis. \*\*\*p < 0.001. (C,D) Loop score of loops anchored at DEGs and stable gene promoters with or without STAG2 enrichment. Loops from *Stag2<sup>f/y</sup>* OLs are used for the analysis in (C) and loops from *Stag2<sup>f/y</sup>;Nes<sup>Cre</sup>* OLs are used for the analysis in (D). Unpaired Wilcoxon test was used for the statistical analysis. \*\*p < 0.01; \*\*\*p < 0.001; ns, not significant. (E) Profile plot of the average enrichment score for the bottom half of each graph panel in Figure 7F. Diagonal pixels were omitted.

Key Resources Table				
Reagent type (species) or resource	Designation	Source or reference	Identifiers	Additional information
strain, strain background (Mus musculus, female)	<i>Stag2</i> <sup>+/-</sup>	This paper		Exon8 of <i>Stag2</i> was targeted by CRISPR-Cas9 (see Materials and Methods Section)
strain, strain background (M. musculus, both sex)	<i>Stag2</i> <sup>f/y</sup> , <i>Stag2</i> <sup>f/f</sup>	This paper		Exon8 of <i>Stag2</i> genomic locus was flanked by loxP sites (see Materials and Methods Section)
strain, strain background (M. musculus, both sex)	C57BL/6J	The Jackson Laboratory	000664; RRID:IMSR_JAX:000664	
strain, strain background (M. musculus, both sex)	B6.129-Gt(ROSA)26Sor <sup>tm1</sup> (cre/ERT2)Tyj/J	The Jackson Laboratory	008463; RRID:IMSR_JAX:008463	
strain, strain background (M. musculus, male)	B6.Cg-Tg(Nes-cre)1Kln/J	The Jackson Laboratory	003771; RRID:IMSR_JAX:003771	
antibody	anti-STAG2 (Rabbit polyclonal)	This paper		The C-terminus recombinant protein of STAG2 ( <i>Homo sapiens</i> ) was used to generate the antibody;

				WB(1:1000)
antibody	anti- $\alpha$ -TUBULIN (Mouse monoclonal)	Sigma-Aldrich	T9026; RRID:AB_477593	WB(1:1000)
antibody	anti-SA1 (Rabbit polyclonal)	Bethyl Laboratories	A302-579A; RRID:AB_2034857	WB(1:1000)
antibody	anti-SMC1 (Rabbit polyclonal)	Bethyl Laboratories	A300-055A RRID:AB_2192467	WB(1:1000)
antibody	anti-SMC3 (Rabbit polyclonal)	Bethyl Laboratories	A300-060A; RRID:AB_67579	WB(1:1000)
antibody	anti-RAD21 (Rabbit polyclonal)	Bethyl Laboratories	A300-080a; RRID:AB_2176615	WB(1:1000)
antibody	anti-MBP (Rat monoclonal)	Abcam	ab7349; RRID:AB_305869	IHC(1:100)
antibody	anti-PLP1 (Rabbit polyclonal)	Abcam	ab28486; RRID:AB_776593	IHC(1:100)
antibody	anti-GFAP (Rabbit polyclonal)	Abcam	ab7260; RRID:AB_305808	IHC(1:100)
antibody	anti-MAP2 (Rabbit polyclonal)	Abcam	ab32454; RRID:AB_776174	IHC(1:50)
antibody	anti-H3K27ac (Rabbit polyclonal)	Abcam	ab4729; RRID:AB_2118291	ChIP(5 $\mu$ l per test)
antibody	anti-O4 Microbeads (Mouse monoclonal)	Miltenyi Biotec	130-094-543; RRID:AB_2847907	MACS(10 $\mu$ l per 10 <sup>7</sup> cells)

antibody	anti-rabbit IgG (H+L), DyLight 800 Conjugate (Goat polyclonal)	Cell Signaling Technology	5151S; RRID:AB_10697505	WB(1:5000)
antibody	anti-mouse IgG (H+L), DyLight 680 Conjugate (Goat polyclonal)	Cell Signaling Technology	5470S; AB_10696895	WB(1:5000)
antibody	anti-rat IgG (H+L), Alexa Fluor 568 (Goat polyclonal)	Thermo Fisher Scientific	A-11077; RRID:AB_2534121	IHC(1:500)
antibody	anti-rabbit IgG (H+L), Alexa Fluor 488 (Goat polyclonal)	Thermo Fisher Scientific	A-11008; RRID:AB_143165	IHC(1:500)
sequence-based reagent	sgRNA#1 target on <i>Stag2</i>	This paper	CRISPR single-guide RNA target sequence	Target sequence: TAGCCAACCTCTTTCTCTATTGG
sequence-based reagent	sgRNA#2 target on <i>Stag2</i>	This paper	CRISPR single-guide RNA target sequence	Target sequence: CAGACAGTATACTGTAATGGAGG
sequence-based reagent	TaqMan probes: <i>Stag2</i>	Thermo Fisher Scientific	Mm01311611_m1	
sequence-based reagent	TaqMan probes: <i>Klk6</i>	Thermo Fisher Scientific	Mm00478322_m1	
sequence-based reagent	TaqMan probes: <i>Ninj2</i>	Thermo Fisher Scientific	Mm00450216_m1	
sequence-based reagent	TaqMan probes: <i>Cpm</i>	Thermo Fisher Scientific	Mm01250802_m1	
sequence-based reagent	TaqMan probes: <i>Fa2h</i>	Thermo Fisher Scientific	Mm00626259_m1	

sequence-based reagent	TaqMan probes: <i>Gapdh</i>	Thermo Fisher Scientific	Mm99999915_g1	
sequence-based reagent	Stag2 gt 5F	This paper	Genotype sequence primers	GGTATTTAC TTGATAGCC AACC
sequence-based reagent	Stag2 gt 5R	This paper	Genotype sequence primers	CTCATCTTGAT TTTCCTGAAGC
sequence-based reagent	Stag2 gt 3F	This paper	Genotype sequence primers	GGTTGAGA CAGACAGTA TAC
sequence-based reagent	Stag2 gt 3R	This paper	Genotype sequence primers	AGGCTGGA CTATGACAA CTC
sequence-based reagent	ISH Probe Stag2 P1 F	This paper	Riboprobe synthesis primers	TACGGTACC GACCTTTCA GATGTCAC CCG
sequence-based reagent	ISH Probe Stag2 P1 R	This paper	Riboprobe synthesis primers	GAAGGATC CGCATCGG ATAGACACT CATGA
sequence-based reagent	ISH Probe Stag2 P2 F	This paper	Riboprobe synthesis primers	TACGGATCC GACCTTTCA GATGTCAC CCG
sequence-based reagent	ISH Probe Stag2 P2 R	This paper	Riboprobe synthesis primers	GAAGGTAC CGCATCGG ATAGACACT CATGA
sequence-based reagent	ISH Probe Stag1 P1 F	This paper	Riboprobe synthesis primers	TTAGGTACC TTACAATGC CTGGTCCTC AGT
sequence-based reagent	ISH Probe Stag1 P1 R	This paper	Riboprobe synthesis primers	GAAGGATC CCTTTCATT GGCTCTCTT CCC
sequence-based reagent	ISH Probe Stag1 P2 F	This paper	Riboprobe synthesis primers	TTAGGATCC TTACAATGC CTGGTCCTC AGT

sequence-based reagent	ISH Probe Stag1 P2 R	This paper	Riboprobe synthesis primers	GAAGGTAC CCTTTCATT GGCTCTCTT CCC
commercial assay or kit	Arima-HiC Kit	Arima Genomics	510008	
chemical compound, drug	Tamoxifen	Sigma-Aldrich	T5648	
chemical compound, drug	4-Hydroxytamoxifen	Sigma-Aldrich	H7904	
software, algorithm	GraphPad Prism	GraphPad Software	RRID:SCR_002798; <a href="https://www.graphpad.com/scientific-software/prism/">https://www.graphpad.com/scientific-software/prism/</a>	
software, algorithm	ImageJ (Fiji)	ImageJ	RRID:SCR_002285; <a href="https://imagej.net/software/fiji/">https://imagej.net/software/fiji/</a>	
software, algorithm	RStudio	The R Foundation	RRID:SCR_000432; <a href="https://www.rstudio.com/">https://www.rstudio.com/</a>	
software, algorithm	Bcl2fastq	Illumina	RRID:SCR_015058	v2.17
software, algorithm	Fastqc	(Andrews 2010); PMID: 24501021	RRID:SCR_014583	v0.11.2
software, algorithm	Fastq_screen	(Wingett 2011)	RRID:SCR_000141; <a href="https://www.bioinformatics.babraham.ac.uk/projects">https://www.bioinformatics.babraham.ac.uk/projects</a>	v0.4.4

			/fastqc/	
software, algorithm	STAR	(Dobin et al. 2013); PMID: 23104886	RRID:SCR_004463; <a href="https://github.com/alexdobin/STAR">https://github.com/alexdobin/STAR</a>	
software, algorithm	FeatureCounts	(Liao, Smyth, and Shi 2014); PMID: 24227677	RRID:SCR_012919; <a href="https://bioconductor.org/packages/release/bioc/html/Rsubread.html">https://bioconductor.org/packages/release/bioc/html/Rsubread.html</a>	
software, algorithm	edgeR	(Robinson, McCarthy, and Smyth 2010); PMID: 19910308	RRID:SCR_012802; <a href="https://bioconductor.org/packages/release/bioc/html/edgeR.html">https://bioconductor.org/packages/release/bioc/html/edgeR.html</a>	
software, algorithm	Ingenuity Pathway Analysis	QIAGEN, (Kramer et al. 2014); PMID: 24336805	RRID:SCR_008653; <a href="https://www.qiagenbioinformatics.com/products/ingenuity-pathway-analysis">https://www.qiagenbioinformatics.com/products/ingenuity-pathway-analysis</a>	
software, algorithm	MACS2	(Zhang et al. 2008); PMID: 18798982	RRID:SCR_013291	v2.0.10
software, algorithm	Bowtie2	(Langmead and Salzberg 2012); PMID: 22388286	RRID:SCR_016368	v2.2.3

software, algorithm	Picard MarkDuplicates	Broad Institute, GitHub Repository	RRID:SCR _006525; <a href="http://broadinstitute.github.io/picard/">http://broadinstitute.github.io/picard/</a>	v1.127
software, algorithm	HOMER	(Heinz et al. 2010, Ross- Innes et al. 2012); PMID: 20513432	RRID:SCR _010881; <a href="http://homer.ucsd.edu/homer/">http://homer.ucsd.edu/homer/</a>	
software, algorithm	Deeptools	(Ramirez et al. 2016); PMID: 27079975	RRID:SCR _016366; <a href="https://deeptools.readthedocs.io/en/develop/">https://deeptools.readthedocs.io/en/develop/</a>	
software, algorithm	Galaxy	(Afgan et al. 2018); PMID: 29790989	RRID:SCR _006281; <a href="https://usegalaxy.org">https://usegalaxy.org</a>	
software, algorithm	Cell Ranger	10x Genomics	RRID:SCR _017344; <a href="https://support.10xgenomics.com/single-cell-gene-expression/software/pipelines/latest/using/mkfastq">https://support.10xgenomics.com/single-cell-gene-expression/software/pipelines/latest/using/mkfastq</a>	
software, algorithm	Seurat	New York Genome Center; (Stuart et al. 2019); PMID: 31178118	RRID:SCR _016341; <a href="https://satijalab.org/seurat">https://satijalab.org/seurat</a>	Satija Lab
software, algorithm	Monocle3	UW Genome Sciences; (Cao et al. 2019); PMID:	RRID:SCR _018685; <a href="https://cole-trapnell-lab.github.io/monocle">https://cole-trapnell-lab.github.io/monocle</a>	Cole Trapnell's Lab

		30787437	3/	
software, algorithm	HiC-Bench pipeline	(Lazaris et al. 2017, Tsirigos et al. 2012); PMID: 22113082	<a href="https://github.com/NYU-BFX/hic-bench">https://github.com/NYU-BFX/hic-bench</a>	
software, algorithm	Juicer “pre” tool	(Durand et al. 2016); PMID: 27467249	RRID:SCR_017226; <a href="https://github.com/aidenlab/juicer">https://github.com/aidenlab/juicer</a>	Aiden Lab
software, algorithm	Juicebox	Aiden Lab, BCM	RRID:SCR_021172; <a href="https://github.com/aidenlab/Juicebox">https://github.com/aidenlab/Juicebox</a>	
software, algorithm	Hic2cool	(Abdennur and Mirny 2020); PMID: 31290943	<a href="https://github.com/4dn-dcic/hic2cool">https://github.com/4dn-dcic/hic2cool</a>	
software, algorithm	pyGenomeTracks	(Lopez-Delisle et al. 2020); PMID: 32745185	<a href="https://github.com/deeptools/pyGenomeTracks">https://github.com/deeptools/pyGenomeTracks</a>	
software, algorithm	Fit-HiC	(Ay, Bailey, and Noble 2014); PMID: 24501021	<a href="https://github.com/ay-lab/fithic">https://github.com/ay-lab/fithic</a>	
software, algorithm	Coolpup.py	(Flyamer, Illingworth, and Bickmore 2020); PMID: 32003791	<a href="https://github.com/open2c/coolpuppy">https://github.com/open2c/coolpuppy</a>	
software, algorithm	clusterProfiler	Bioinformatics Group, Southern Medical	RRID:SCR_016884; <a href="https://github.com/Yu">https://github.com/Yu</a>	

		University; (Wu et al. 2021); PMID: 34557778	Lab- SMU/clust erProfiler	
software, algorithm	HiC-Pro	(Servant et al. 2015); PMID: 26619908	RRID:SCR _017643	v3.1.0
software, algorithm	HiCRep	(Yang et al. 2017); PMID: 28855260	<a href="https://github.com/TaoYang-dev/hicrep">https://github.com/TaoYang-dev/hicrep</a>	
software, algorithm	GENOVA	(van der Weide et al. 2021); PMID: 34046591	<a href="https://github.com/robinweide/GENOVA">https://github.com/robinweide/GENOVA</a>	

## References

- Abdennur, N., and L. A. Mirny. 2020. "Cooler: scalable storage for Hi-C data and other genomically labeled arrays." *Bioinformatics* 36 (1):311-316. doi: 10.1093/bioinformatics/btz540.
- Afgan, E., D. Baker, B. Batut, M. van den Beek, D. Bouvier, M. Cech, J. Chilton, D. Clements, N. Coraor, B. A. Gruning, A. Guerler, J. Hillman-Jackson, S. Hiltemann, V. Jalili, H. Rasche, N. Soranzo, J. Goecks, J. Taylor, A. Nekrutenko, and D. Blankenberg. 2018. "The Galaxy platform for accessible, reproducible and collaborative biomedical analyses: 2018 update." *Nucleic Acids Res* 46 (W1):W537-W544. doi: 10.1093/nar/gky379.
- Andrews, Simon. 2010. "FastQC: a quality control tool for high throughput sequence data." <http://www.bioinformatics.babraham.ac.uk/projects/fastqc>.
- Ay, F., T. L. Bailey, and W. S. Noble. 2014. "Statistical confidence estimation for Hi-C data reveals regulatory chromatin contacts." *Genome Res* 24 (6):999-1011. doi: 10.1101/gr.160374.113.
- Cao, J., M. Spielmann, X. Qiu, X. Huang, D. M. Ibrahim, A. J. Hill, F. Zhang, S. Mundlos, L. Christiansen, F. J. Steemers, C. Trapnell, and J. Shendure. 2019. "The single-cell transcriptional landscape of mammalian organogenesis." *Nature* 566 (7745):496-502. doi: 10.1038/s41586-019-0969-x.
- Dobin, A., C. A. Davis, F. Schlesinger, J. Drenkow, C. Zaleski, S. Jha, P. Batut, M. Chaisson, and T. R. Gingeras. 2013. "STAR: ultrafast universal RNA-seq aligner." *Bioinformatics* 29 (1):15-21. doi: 10.1093/bioinformatics/bts635.
- Durand, N. C., M. S. Shamim, I. Machol, S. S. Rao, M. H. Huntley, E. S. Lander, and E. L. Aiden. 2016. "Juicer Provides a One-Click System for Analyzing Loop-Resolution Hi-C Experiments." *Cell Syst* 3 (1):95-8. doi: 10.1016/j.cels.2016.07.002.
- Flyamer, I. M., R. S. Illingworth, and W. A. Bickmore. 2020. "Coolpup.py: versatile pile-up analysis of Hi-C data." *Bioinformatics* 36 (10):2980-2985. doi: 10.1093/bioinformatics/btaa073.
- Heinz, S., C. Benner, N. Spann, E. Bertolino, Y. C. Lin, P. Laslo, J. X. Cheng, C. Murre, H. Singh, and C. K. Glass. 2010. "Simple combinations of lineage-determining

- transcription factors prime cis-regulatory elements required for macrophage and B cell identities." *Mol Cell* 38 (4):576-89. doi: 10.1016/j.molcel.2010.05.004.
- Kramer, A., J. Green, J. Pollard, Jr., and S. Tugendreich. 2014. "Causal analysis approaches in Ingenuity Pathway Analysis." *Bioinformatics* 30 (4):523-30. doi: 10.1093/bioinformatics/btt703.
- Langmead, B., and S. L. Salzberg. 2012. "Fast gapped-read alignment with Bowtie 2." *Nat Methods* 9 (4):357-9. doi: 10.1038/nmeth.1923.
- Lazaris, C., S. Kelly, P. Ntziachristos, I. Aifantis, and A. Tsigos. 2017. "HiC-bench: comprehensive and reproducible Hi-C data analysis designed for parameter exploration and benchmarking." *BMC Genomics* 18 (1):22. doi: 10.1186/s12864-016-3387-6.
- Liao, Y., G. K. Smyth, and W. Shi. 2014. "featureCounts: an efficient general purpose program for assigning sequence reads to genomic features." *Bioinformatics* 30 (7):923-30. doi: 10.1093/bioinformatics/btt656.
- Lopez-Delisle, L., L. Rabbani, J. Wolff, V. Bhardwaj, R. Backofen, B. Gruning, F. Ramirez, and T. Manke. 2020. "pyGenomeTracks: reproducible plots for multivariate genomic data sets." *Bioinformatics*. doi: 10.1093/bioinformatics/btaa692.
- Ramirez, F., D. P. Ryan, B. Gruning, V. Bhardwaj, F. Kilpert, A. S. Richter, S. Heyne, F. Dundar, and T. Manke. 2016. "deepTools2: a next generation web server for deep-sequencing data analysis." *Nucleic Acids Res* 44 (W1):W160-5. doi: 10.1093/nar/gkw257.
- Robinson, M. D., D. J. McCarthy, and G. K. Smyth. 2010. "edgeR: a Bioconductor package for differential expression analysis of digital gene expression data." *Bioinformatics* 26 (1):139-40. doi: 10.1093/bioinformatics/btp616.
- Ross-Innes, C. S., R. Stark, A. E. Teschendorff, K. A. Holmes, H. R. Ali, M. J. Dunning, G. D. Brown, O. Gojis, I. O. Ellis, A. R. Green, S. Ali, S. F. Chin, C. Palmieri, C. Caldas, and J. S. Carroll. 2012. "Differential oestrogen receptor binding is associated with clinical outcome in breast cancer." *Nature* 481 (7381):389-93. doi: 10.1038/nature10730.
- Servant, N., N. Varoquaux, B. R. Lajoie, E. Viara, C. J. Chen, J. P. Vert, E. Heard, J. Dekker, and E. Barillot. 2015. "HiC-Pro: an optimized and flexible pipeline for Hi-C data processing." *Genome Biol* 16:259. doi: 10.1186/s13059-015-0831-x.
- Stuart, T., A. Butler, P. Hoffman, C. Hafemeister, E. Papalexi, W. M. Mauck, 3rd, Y. Hao, M. Stoeckius, P. Smibert, and R. Satija. 2019. "Comprehensive Integration of Single-Cell Data." *Cell* 177 (7):1888-1902 e21. doi: 10.1016/j.cell.2019.05.031.
- Tsigos, A., N. Haiminen, E. Bilal, and F. Utro. 2012. "GenomicTools: a computational platform for developing high-throughput analytics in genomics." *Bioinformatics* 28 (2):282-3. doi: 10.1093/bioinformatics/btr646.
- van der Weide, R. H., T. van den Brand, J. H. I. Haarhuis, H. Teunissen, B. D. Rowland, and E. de Wit. 2021. "Hi-C analyses with GENOVA: a case study with cohesin variants." *NAR Genom Bioinform* 3 (2):lqab040. doi: 10.1093/nargab/lqab040.
- Wingett, Steven. 2011. "FastQ Screen: quality control tool to screen a library of sequences in FastQ format against a set of sequence databases. ." [http://www.bioinformatics.babraham.ac.uk/projects/fastq\\_screen](http://www.bioinformatics.babraham.ac.uk/projects/fastq_screen)
- Wu, T., E. Hu, S. Xu, M. Chen, P. Guo, Z. Dai, T. Feng, L. Zhou, W. Tang, L. Zhan, X. Fu, S. Liu, X. Bo, and G. Yu. 2021. "clusterProfiler 4.0: A universal enrichment tool for interpreting omics data." *Innovation (N Y)* 2 (3):100141. doi: 10.1016/j.xinn.2021.100141.
- Yang, T., F. Zhang, G. G. Yardimci, F. Song, R. C. Hardison, W. S. Noble, F. Yue, and Q. Li. 2017. "HiCRep: assessing the reproducibility of Hi-C data using a stratum-adjusted correlation coefficient." *Genome Res* 27 (11):1939-1949. doi: 10.1101/gr.220640.117.
- Zhang, Y., T. Liu, C. A. Meyer, J. Eeckhoutte, D. S. Johnson, B. E. Bernstein, C. Nusbaum, R. M. Myers, M. Brown, W. Li, and X. S. Liu. 2008. "Model-based analysis of ChIP-Seq (MACS)." *Genome Biol* 9 (9):R137. doi: 10.1186/gb-2008-9-9-r137.



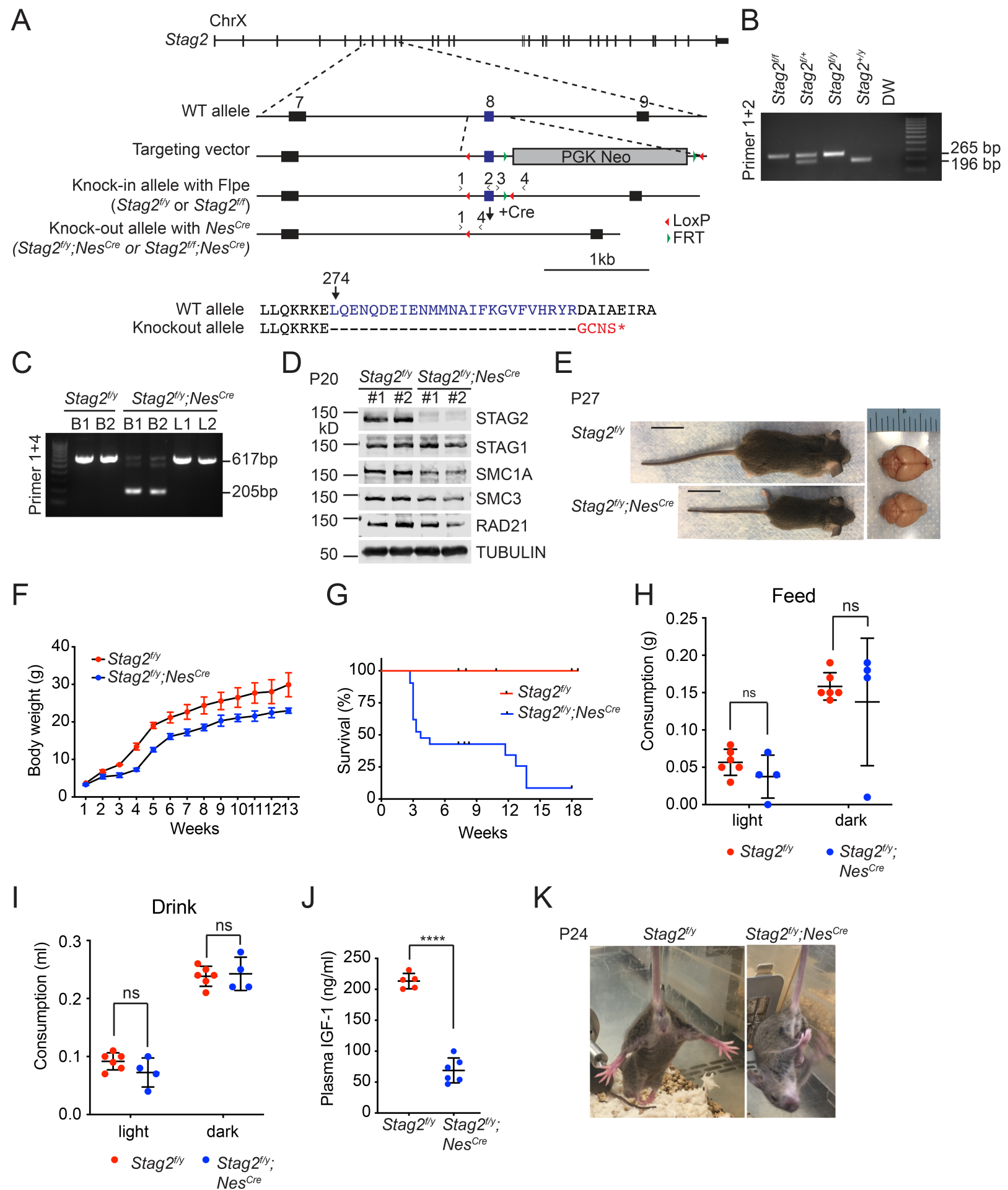


**Figure 1**

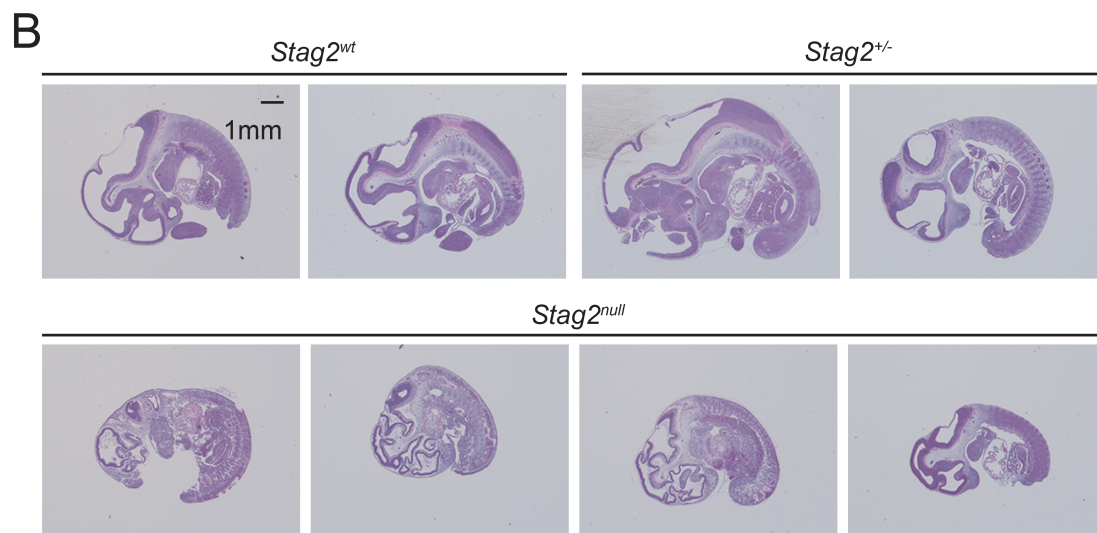
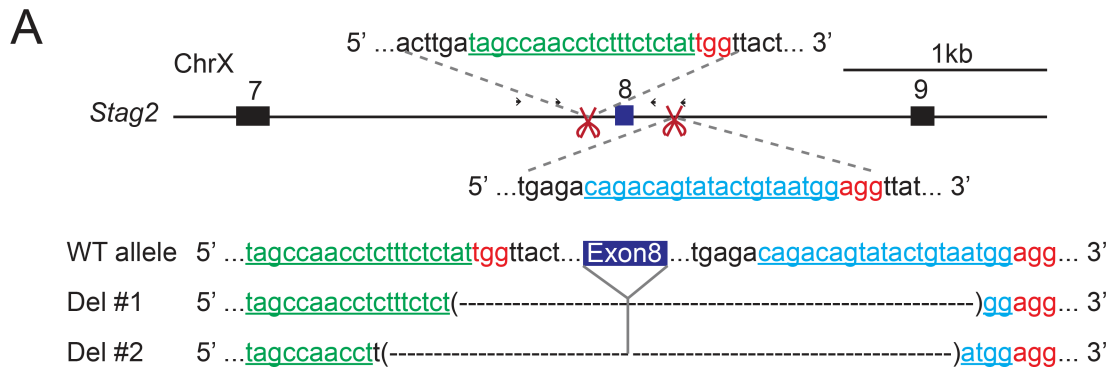


**Figure 1—Figure Supplement 1**

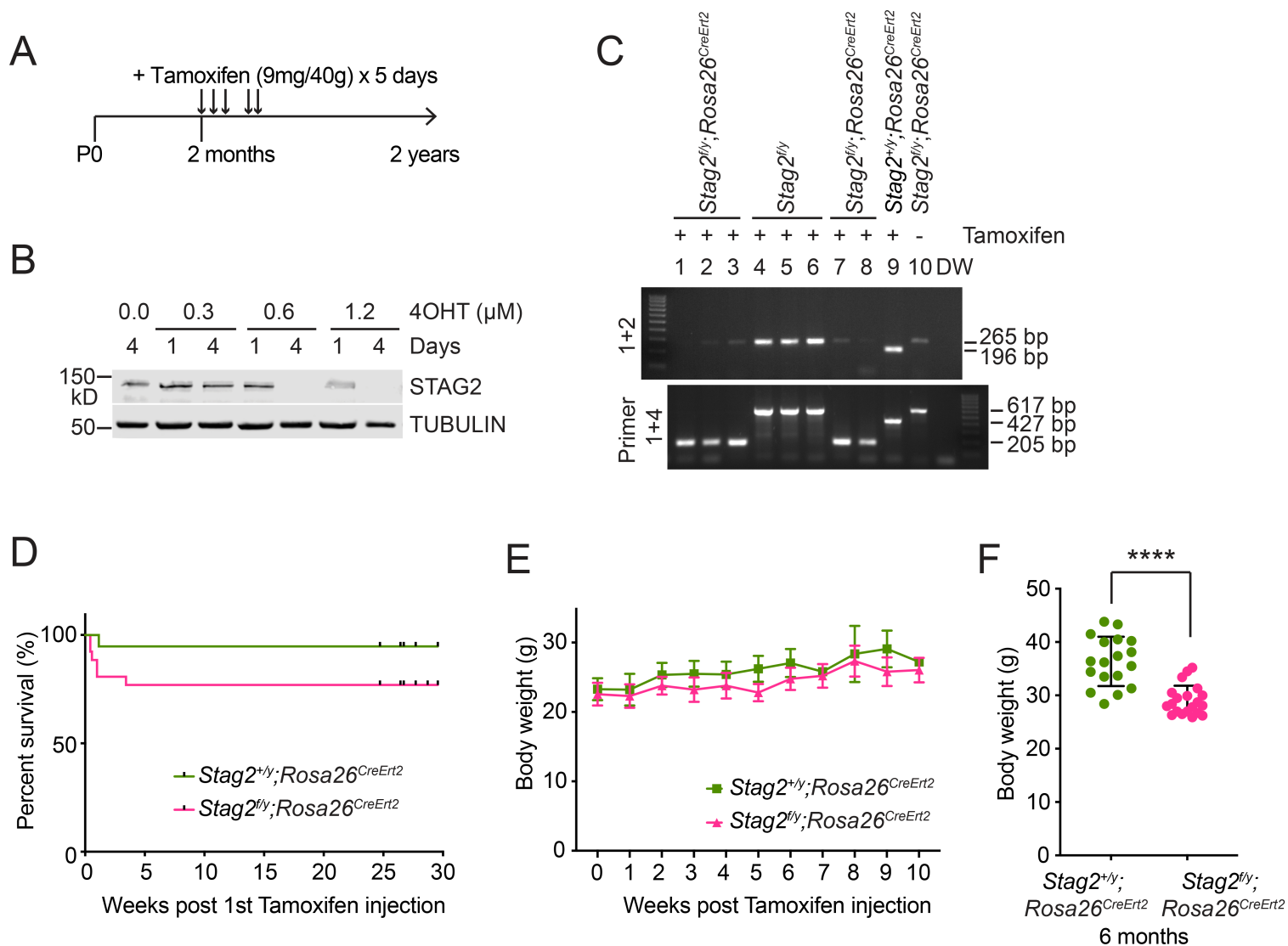
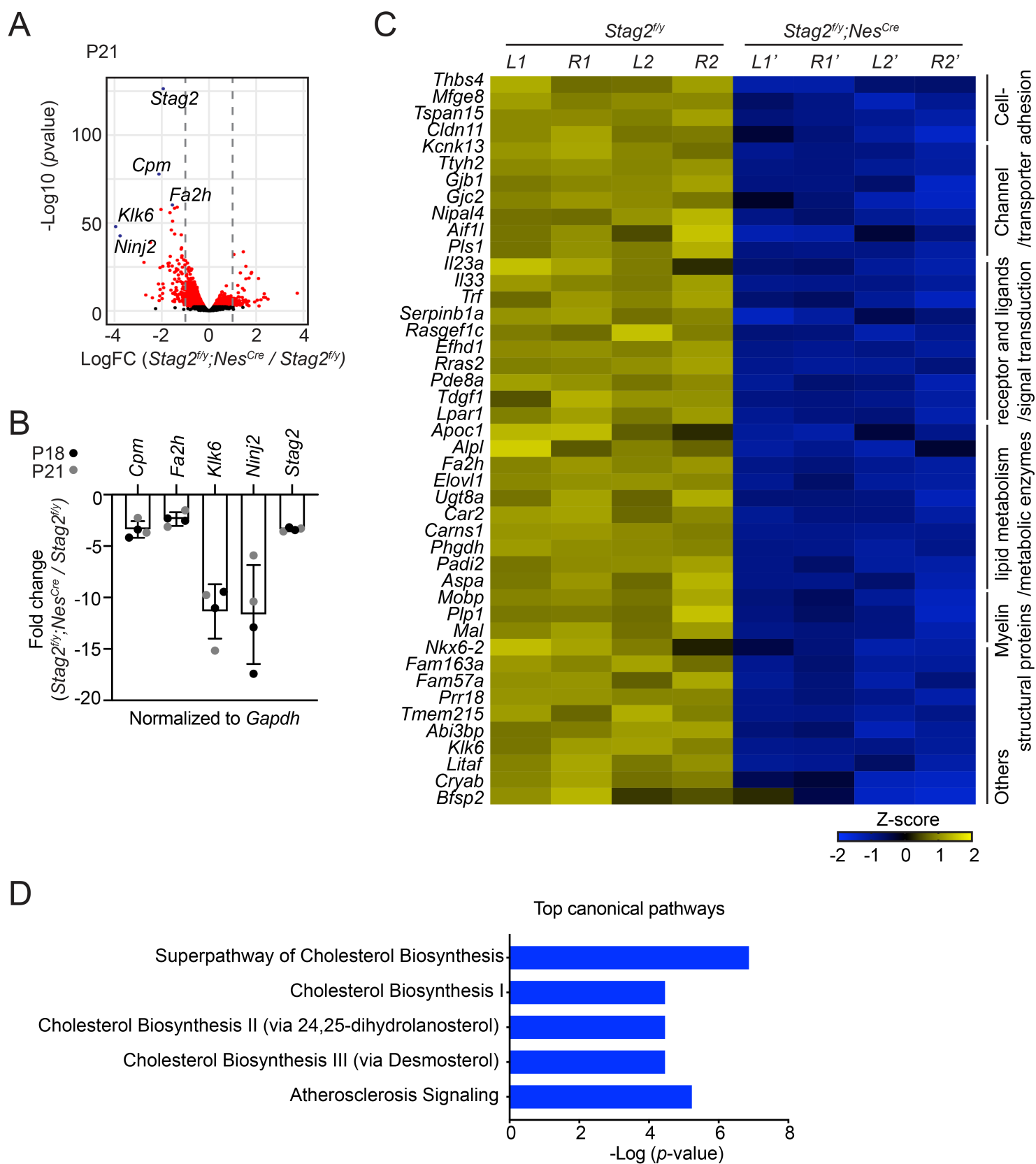
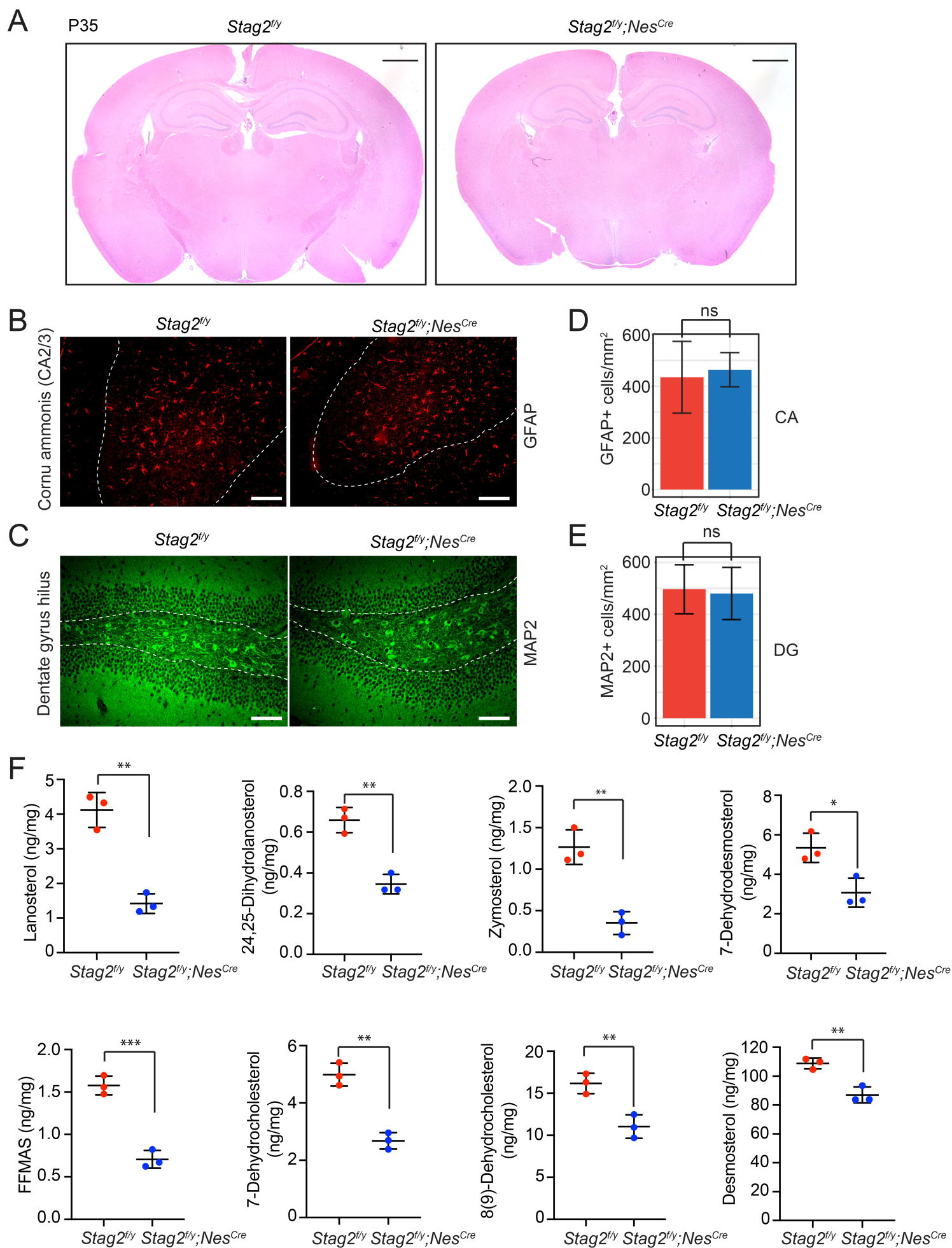


Figure 1—Figure Supplement 2



**Figure 2**



**Figure 2—Figure Supplement 1**

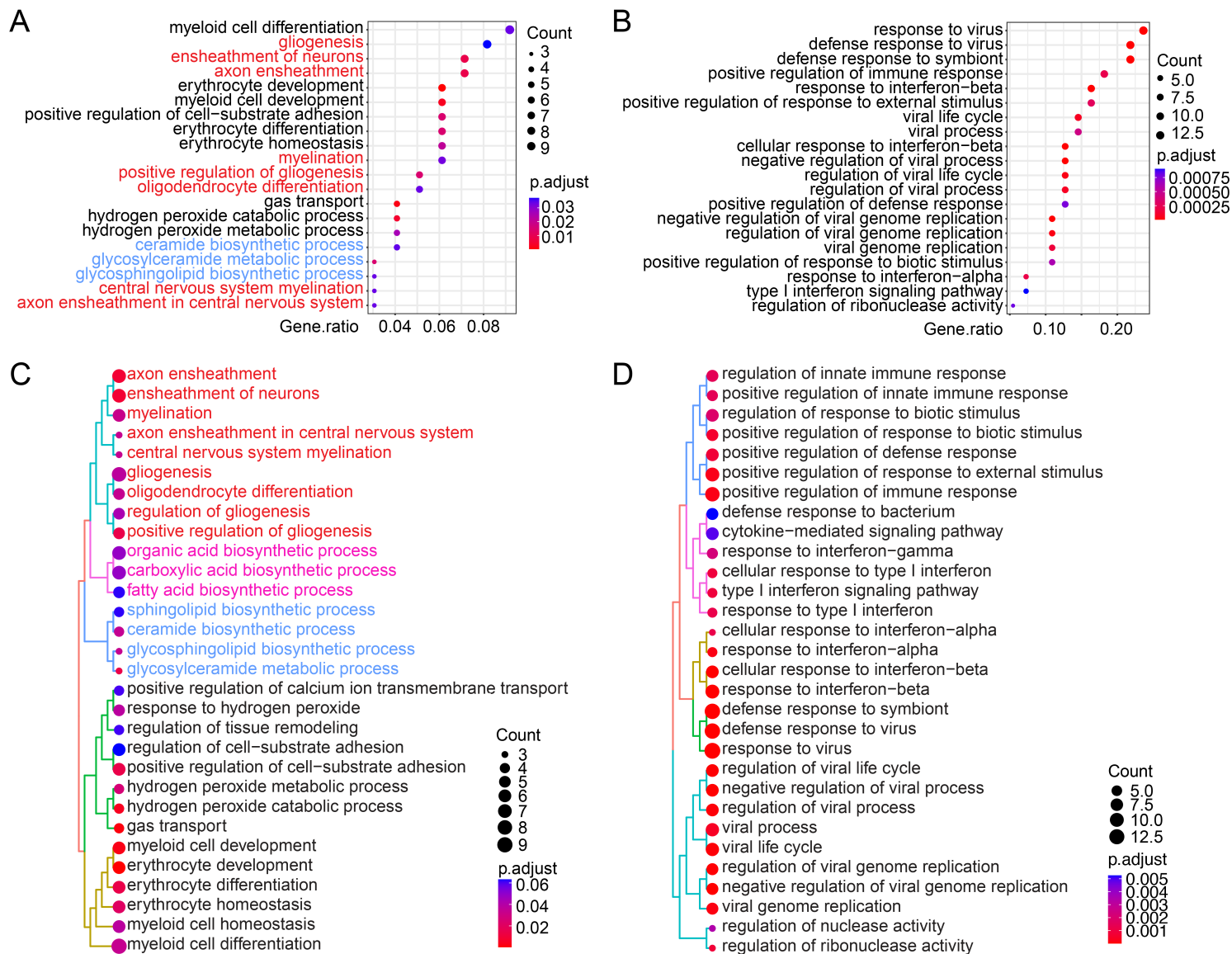
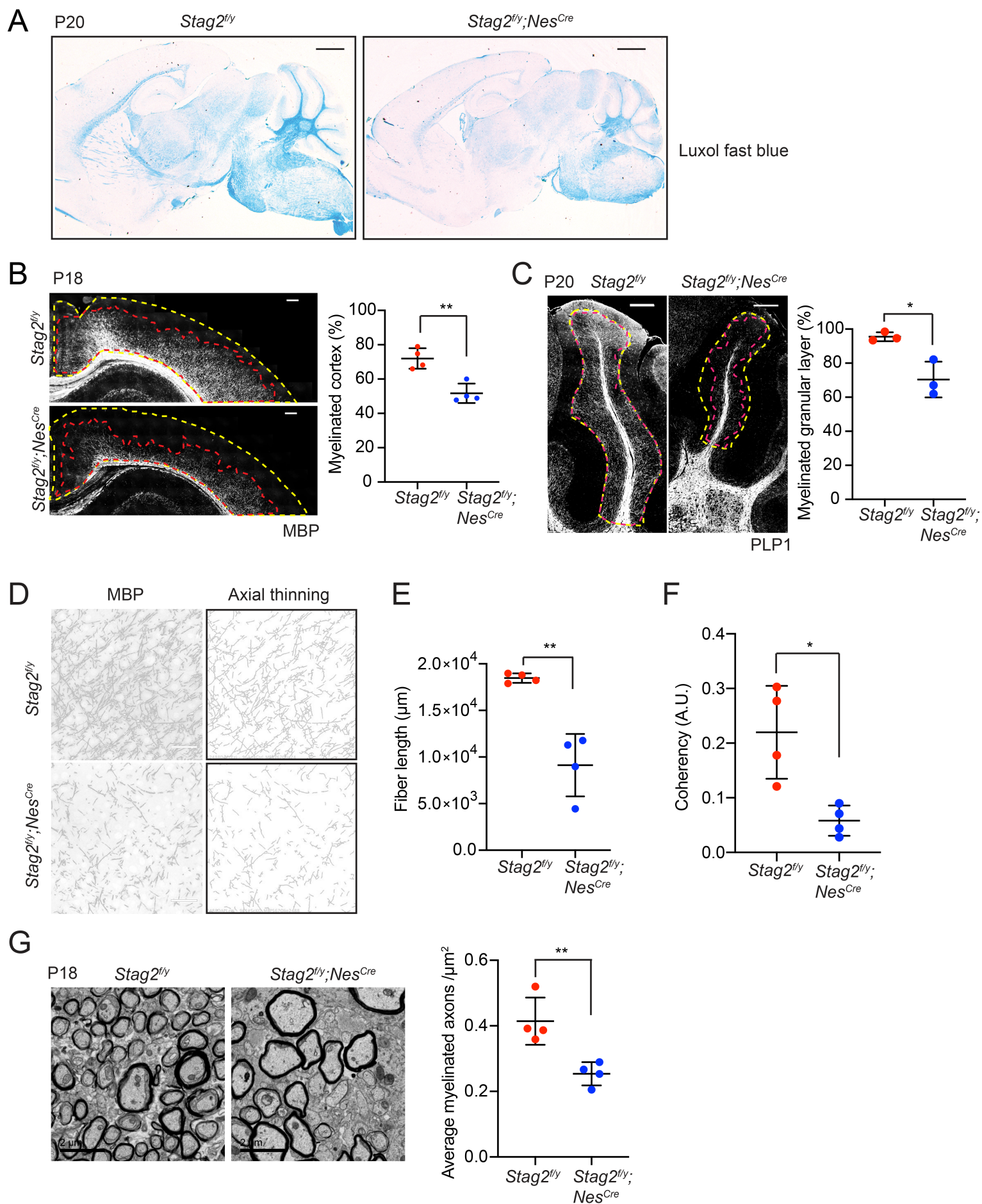
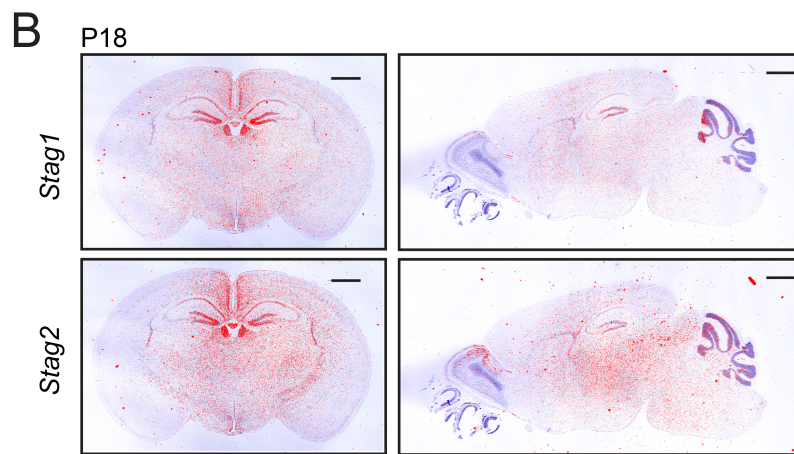
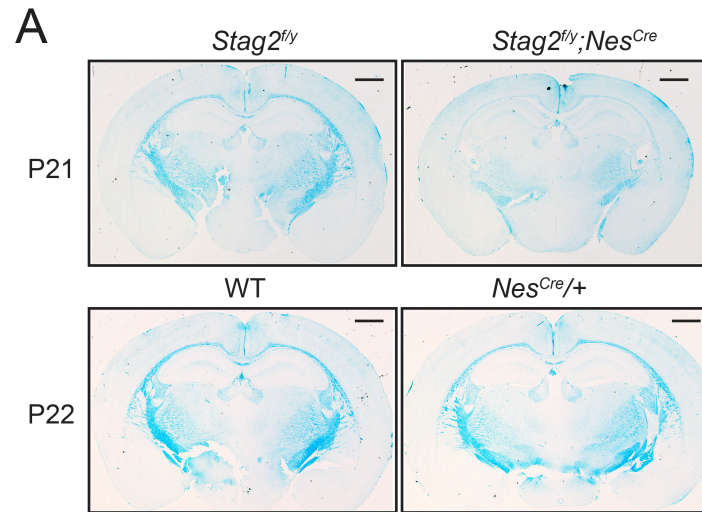


Figure 2—Figure Supplement 2



**Figure 3**



**Figure 3—Figure Supplement 1**

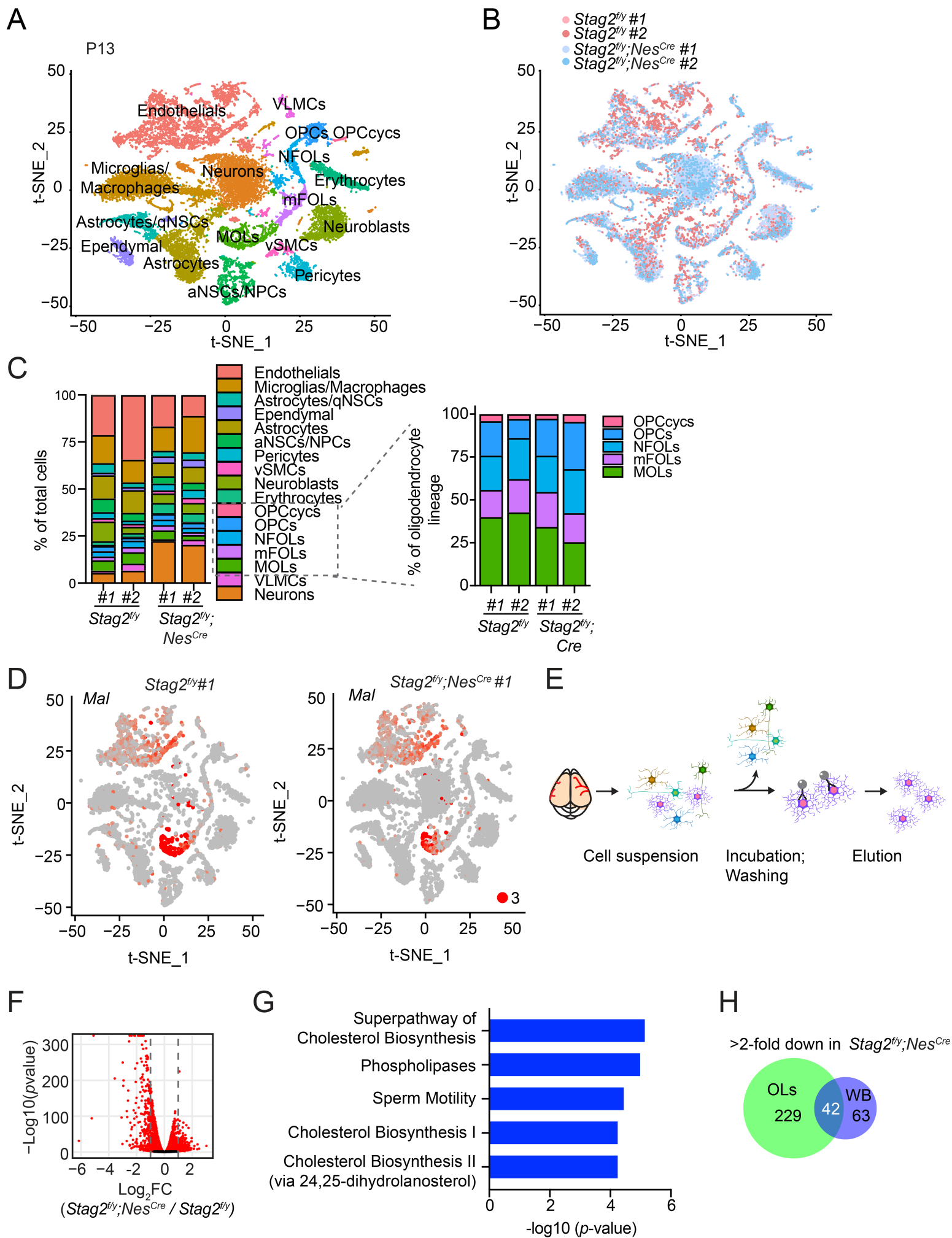
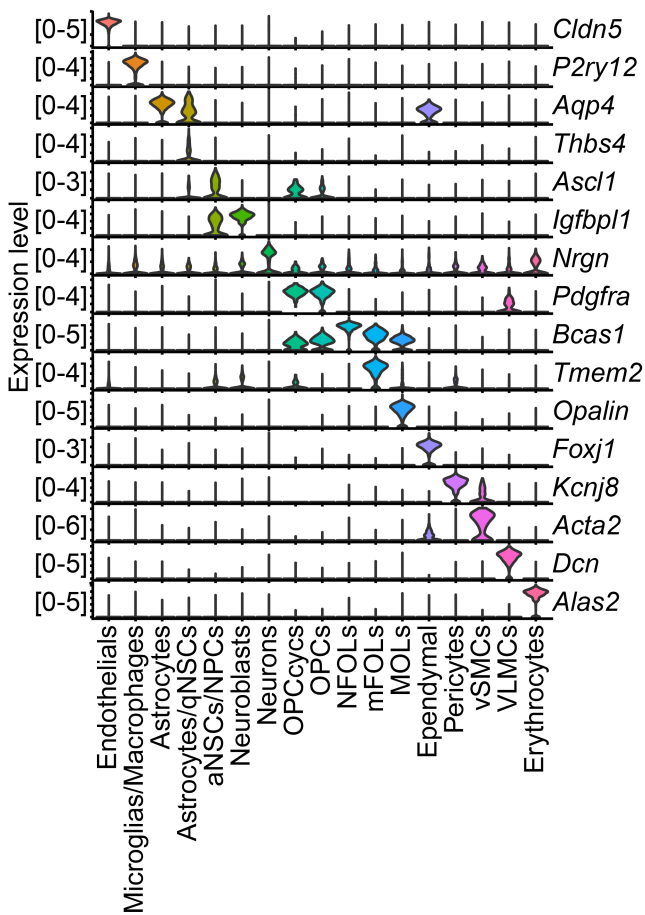
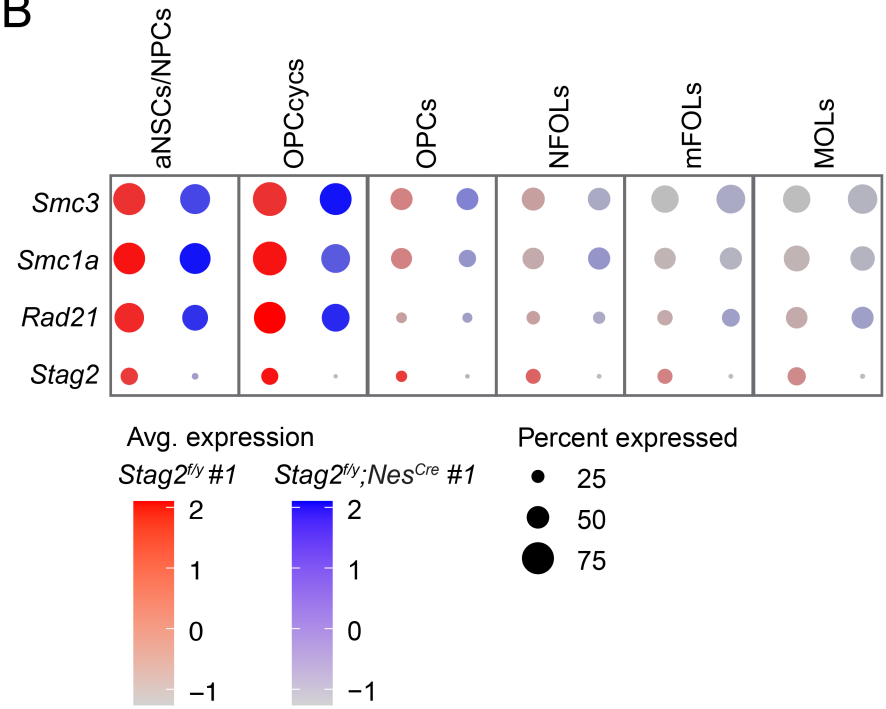


**Figure 4**

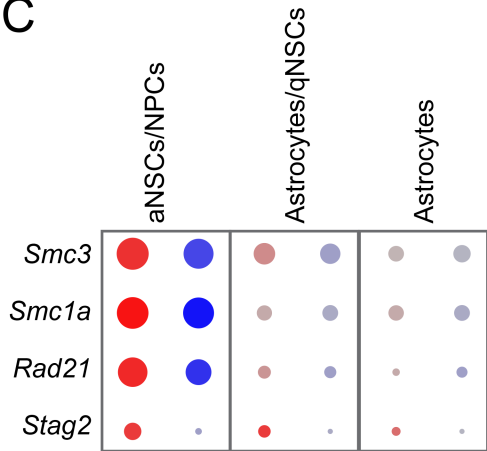
A



B



C



D

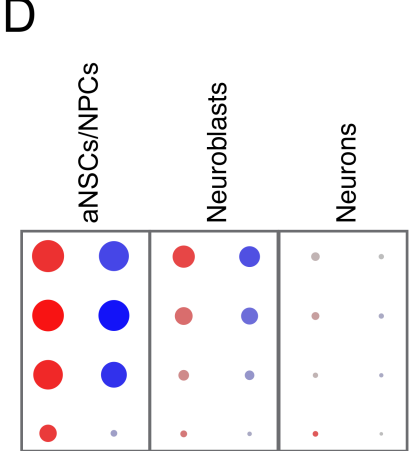
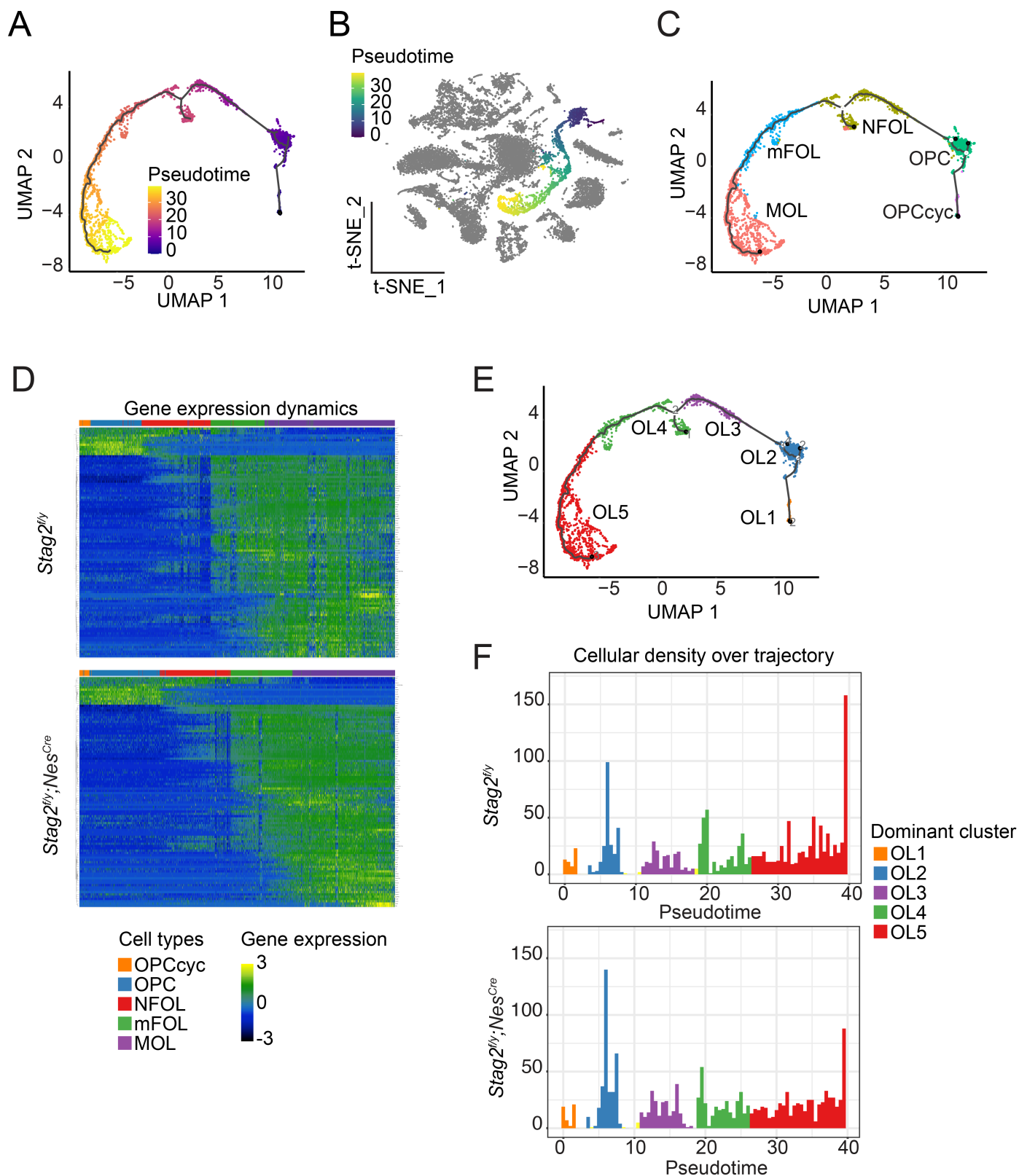
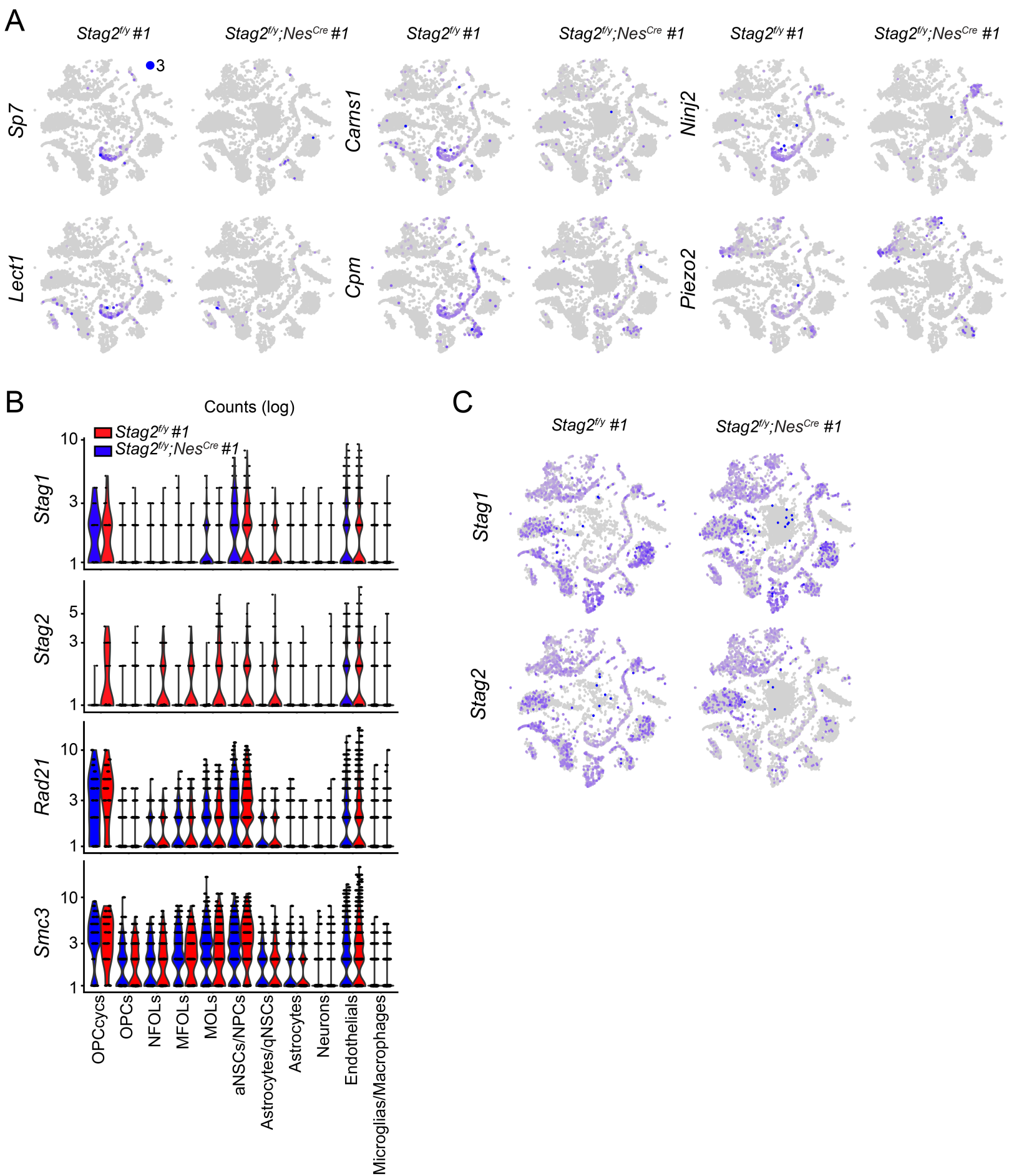


Figure 4—Figure Supplement 1



**Figure 4—Figure Supplement 2**



**Figure 4—Figure Supplement 3**

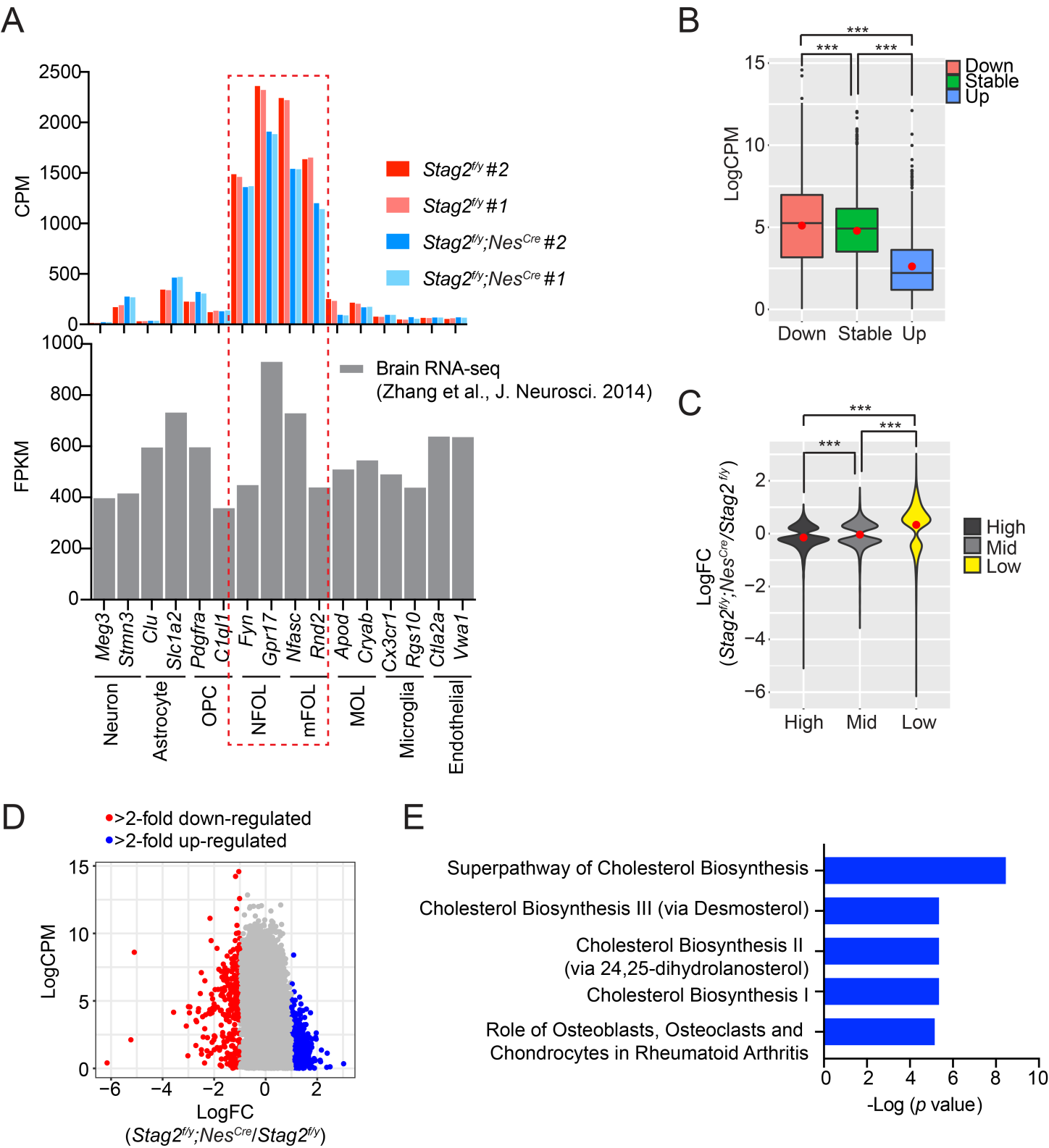


Figure 4—Figure Supplement 4

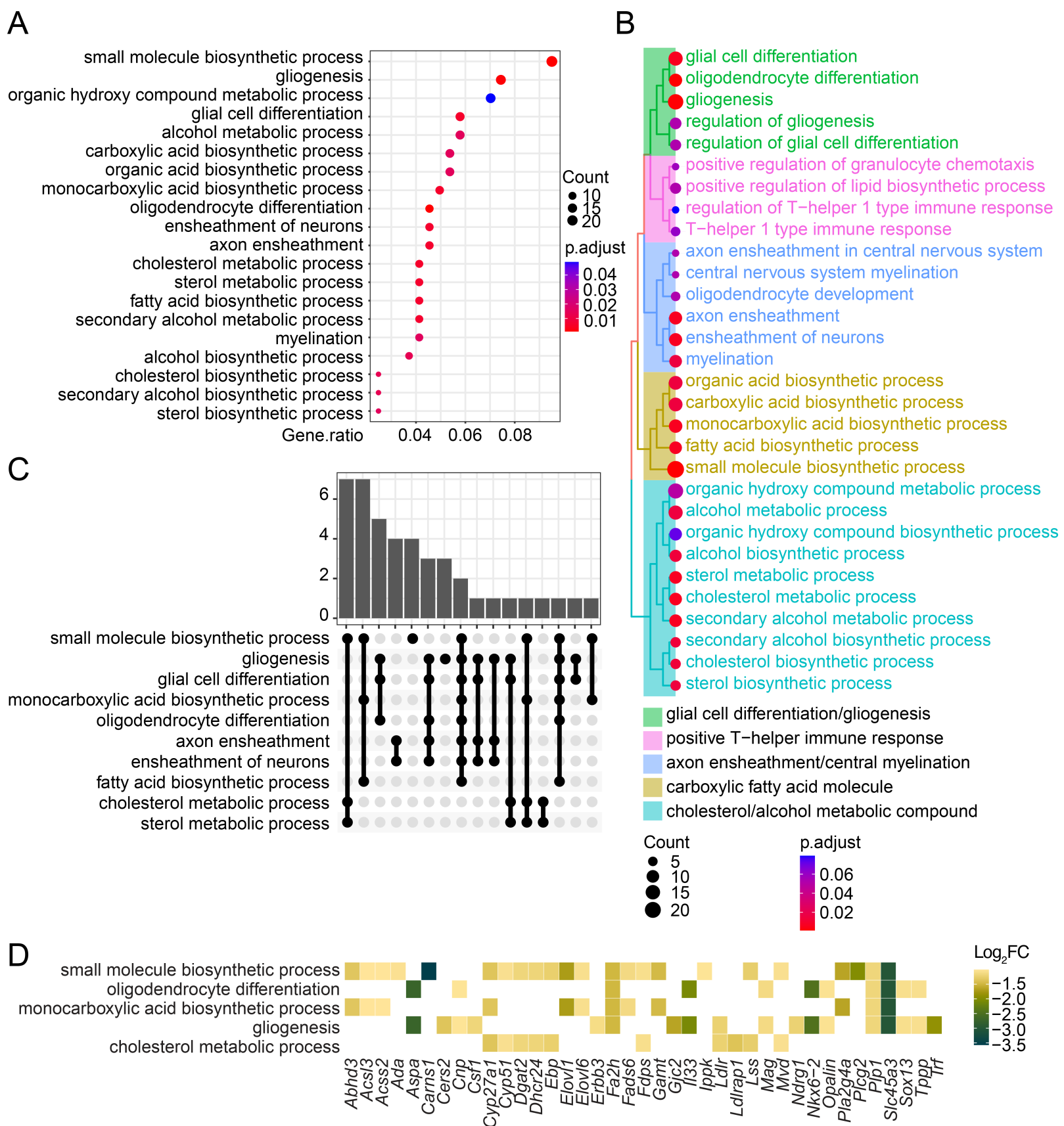
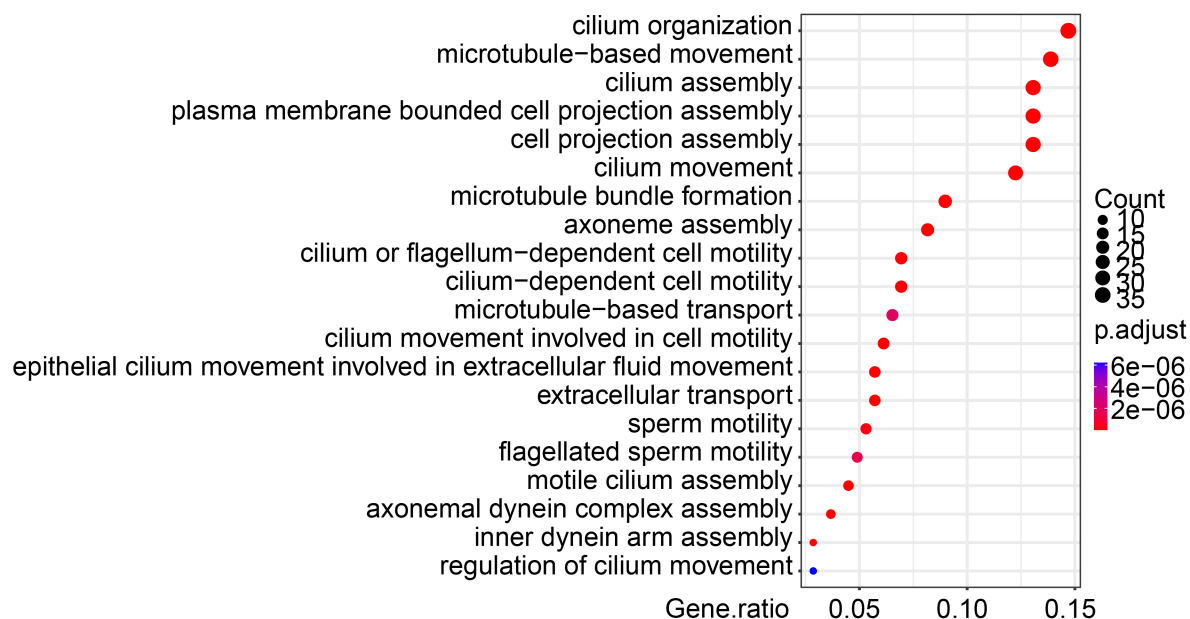
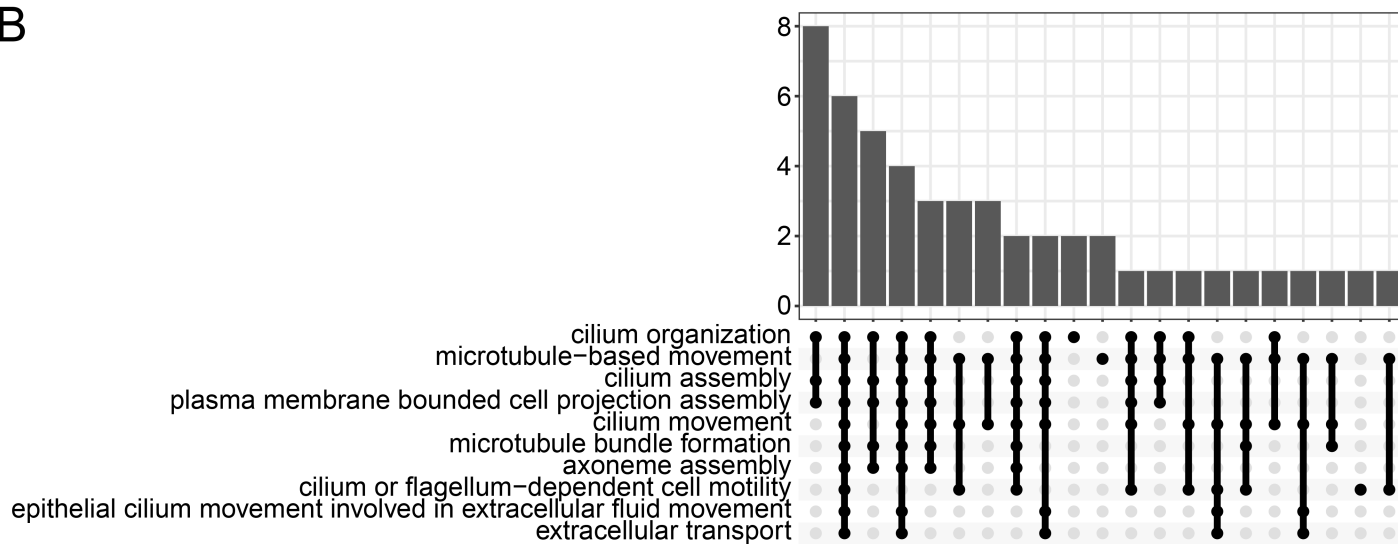


Figure 4—Figure Supplement 5

A



B



C

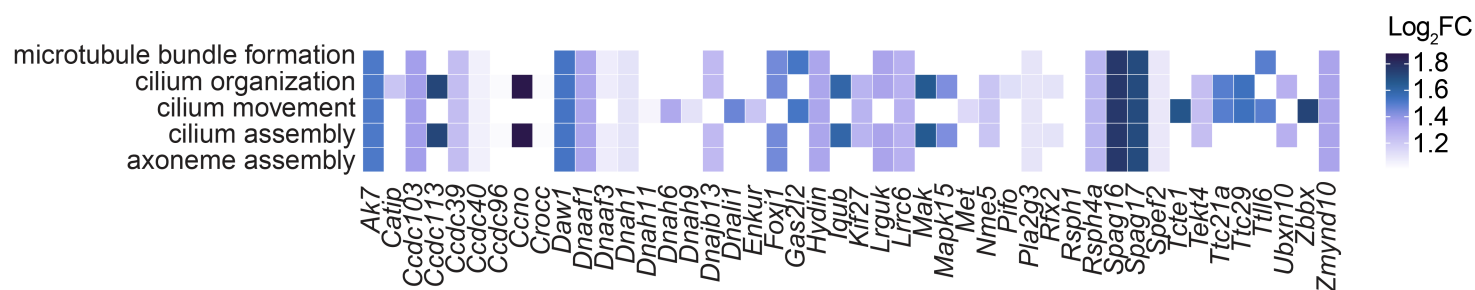
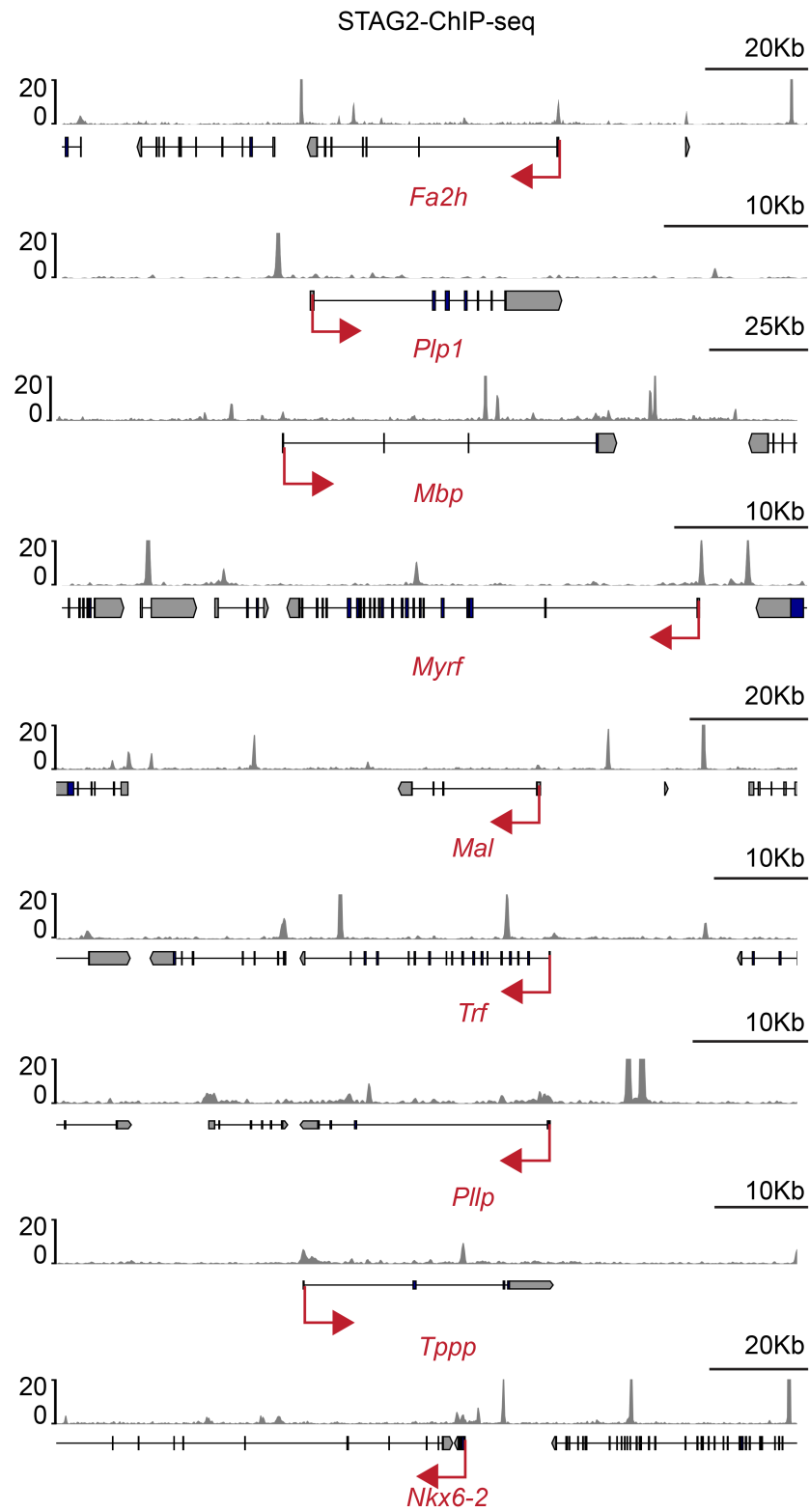
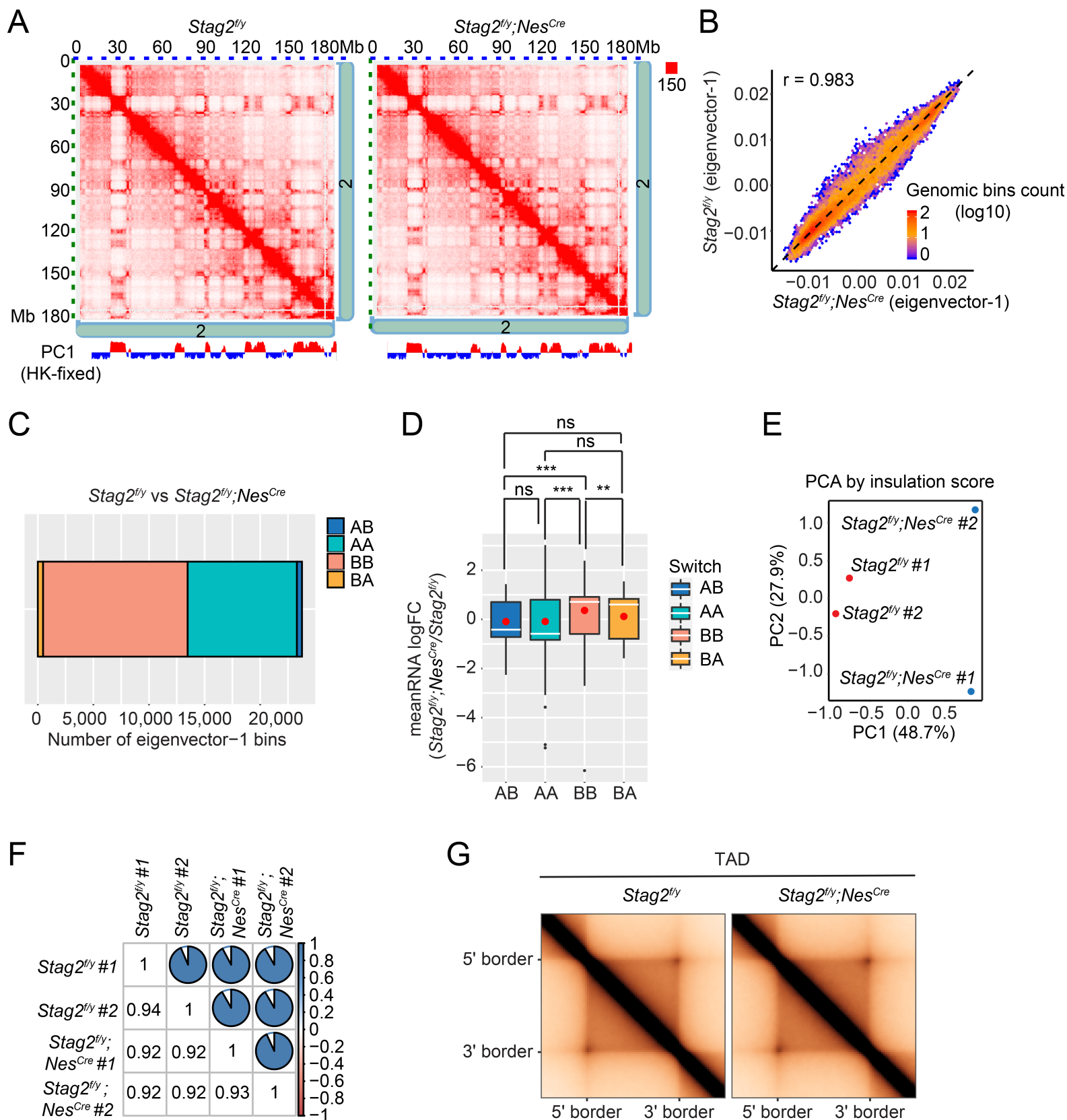


Figure 4—Figure Supplement 6





**Figure 5—Figure Supplement 1**



**Figure 6**

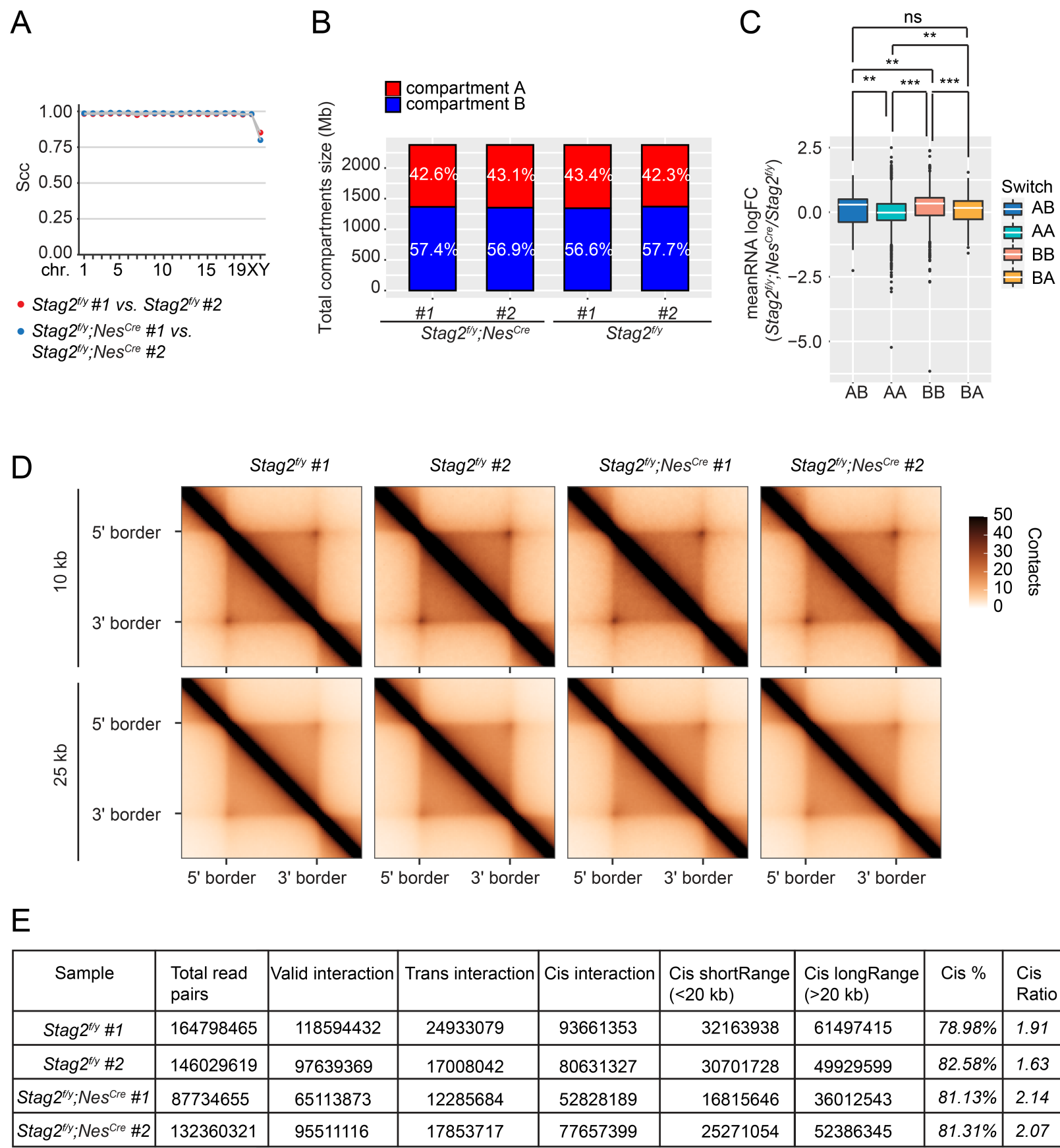


## Figure 6—Figure Supplement 1

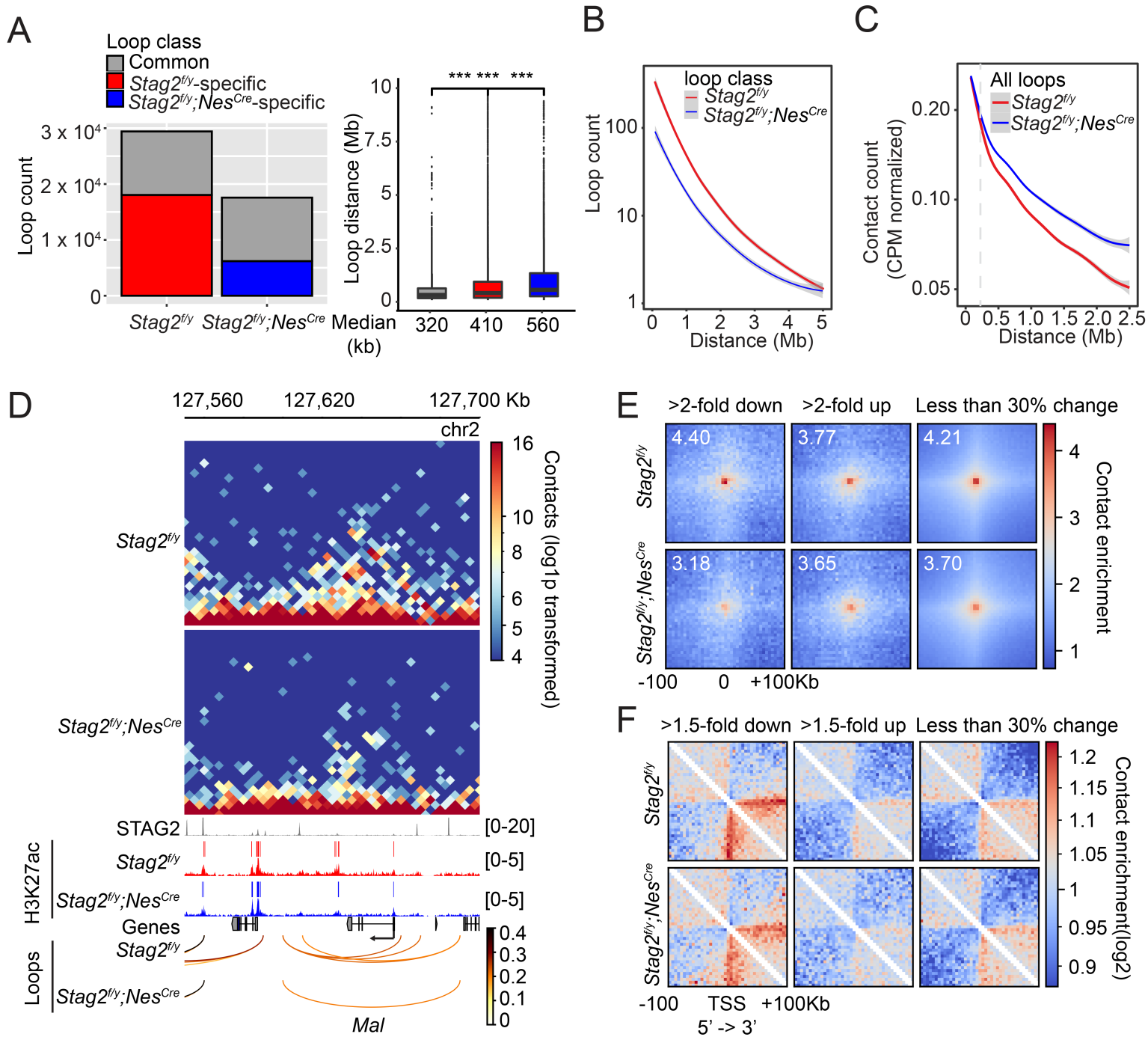


**Figure 7**

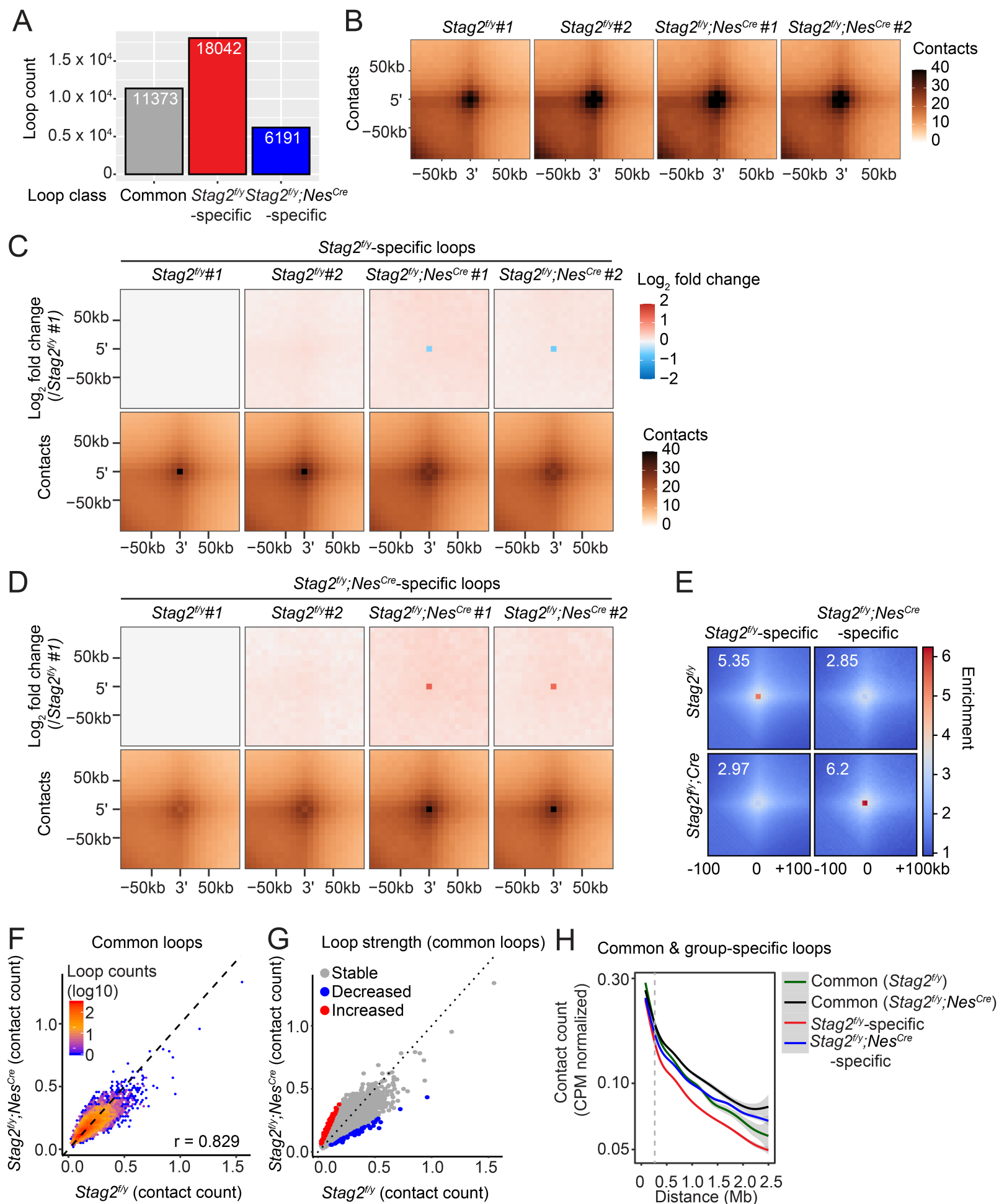
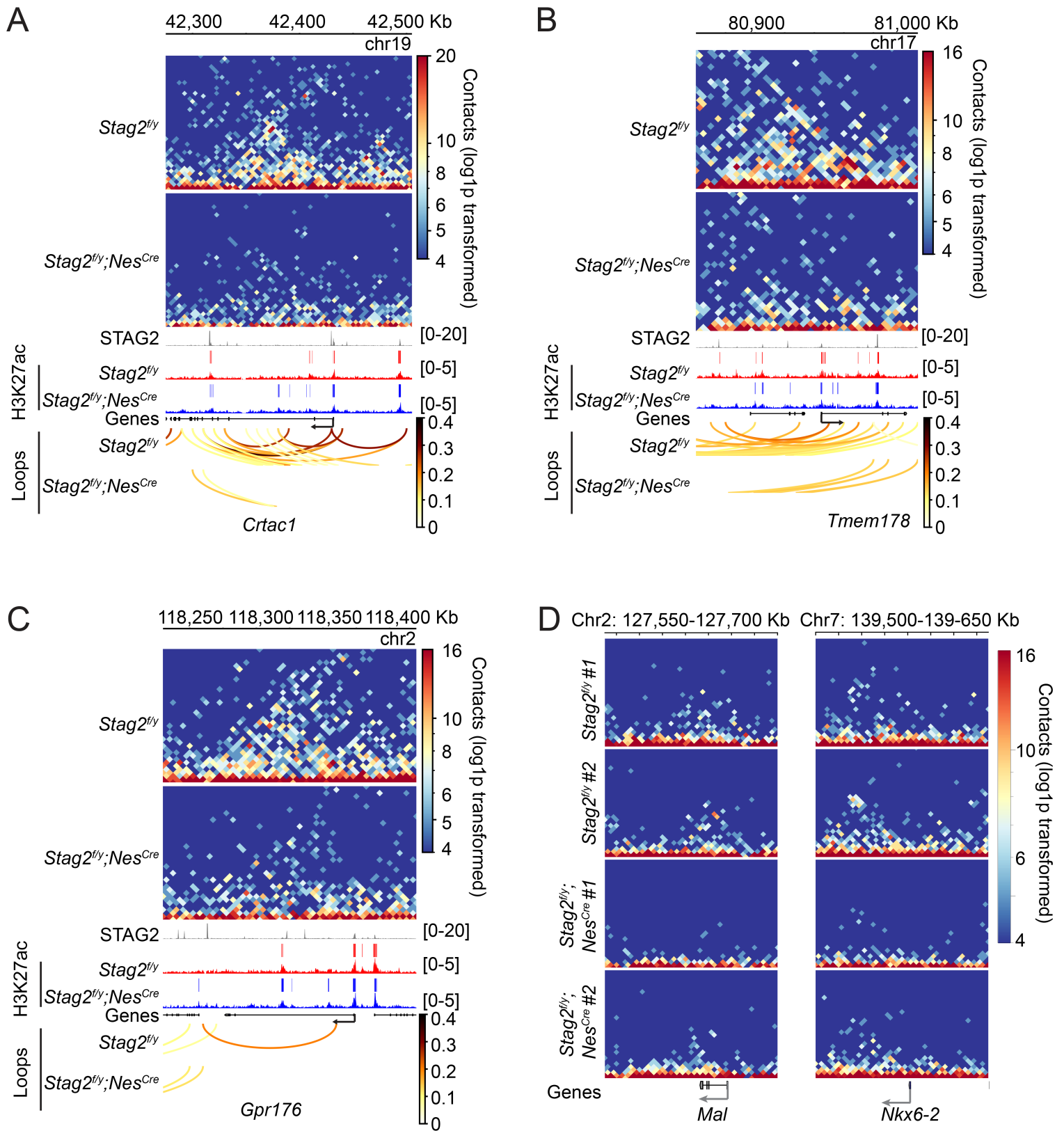
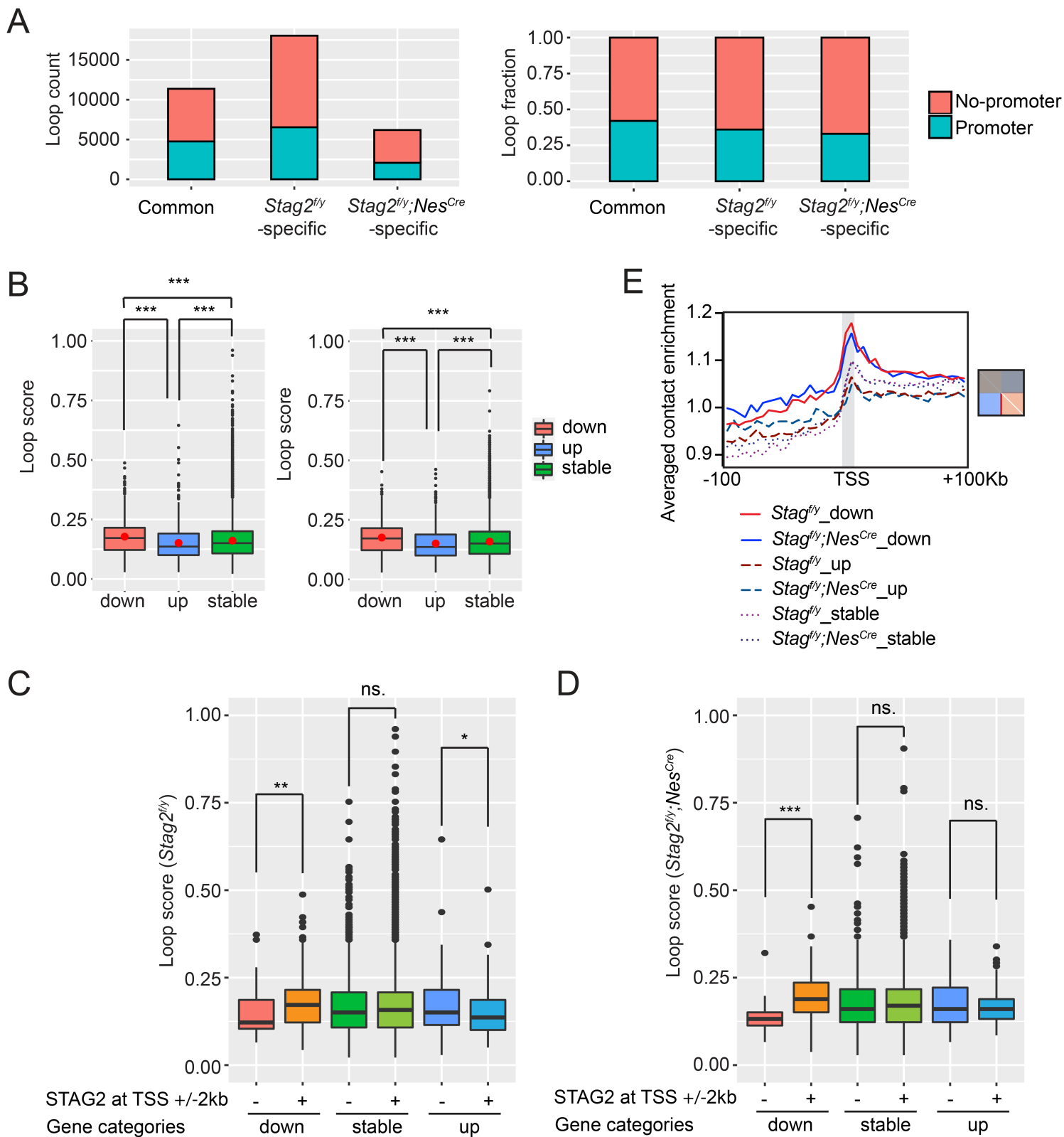


Figure 7—Figure Supplement 1

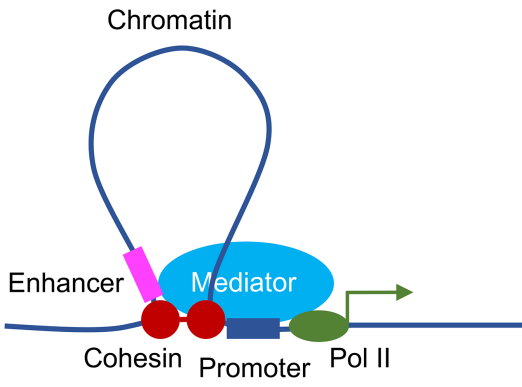


**Figure 7—Figure Supplement 2**



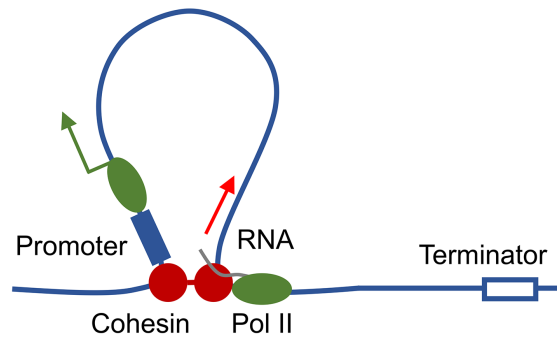
**Figure 7—Figure Supplement 3**

A



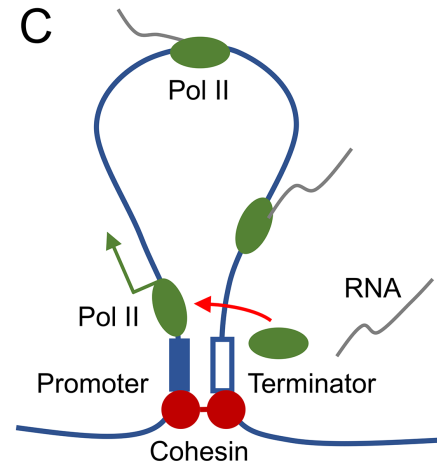
Promoter-enhancer loop

B



Promoter-gene loop

C



Gene loop

Figure 8